LA-UR-05-8002

Approved for public release; distribution is unlimited.

Title:	Calculation Verification: Pointwise Estimation of Solutions and Their Method-Associated Numerical Error, LA-UR-05-8002, 2005.
Author(s):	David Pamer Smitherman (X-7) James R. Kamm (X-7) Jerry S. Brock (X-7)
Date:	October 19, 2005

Calculation Verification: Pointwise Estimation of Solutions and Their Method-Associated Numerical Error

In Support of FY05 Q4 ASC Verification Level 2 Milestone

David Palmer Smitherman, James R. Kamm, and Jerry S. Brock
Los Alamos National Laboratory

Abstract

The standard approach to conducting verification analysis using complex physics problems with no exact solution presents two significant limitations. Computational solutions that converge by oscillation are not calculable and the technique is limited to a simple error ansatz. An improvement to the current method is presented. The absolute value of the pointwise error is calculated, allowing for local oscillatory convergence. The equations are then solved using Newton's method for the convergence constants and an estimated exact solution simultaneously. This procedure allows for a more complex ansatz if desired. The improved method was tested on four pure hydrodynamics problems using the Eulerian code RAGE. A linear acoustic wave and a 1D Riemann problem have exact mathematical solutions, which were compared to the estimated solution. A nonlinear acoustic wave and 2D Riemann problem have no exact solutions, but the estimated solution was shown to be useful in providing a more accurate solution on a coarse grid than the calculated solution. In addition, the method was able to calculate the convergence of oscillatory points at the discontinuities.

Contents

List of Tables

List of Figures

1. Introduction

An important element of verification activities is the quantitative evaluation and analysis of the error between computed and exact solutions for well-defined problems.[1] This approach, known as *code verification*, is based on several assumptions that constrain the nature of the analysis. The quantitative analysis is based on an ansatz for the discretization error; equally important is the further supposition that an exact solution is known and available for the problem of interest. An alternative approach, *calculation verification*, quantifies the self-convergence through an error ansatz with an estimated exact solution standing in for the exact solution.[2] Normally, the estimated exact solution is not calculated directly. Both approaches provide quantitative convergence rates for a code on the problem of interest. These approaches, though limited, have proved to be fruitful methods both for identifying code shortcomings (e.g., software bugs or limitations of numerical methods) and for providing quantitative evidence in support of software quality.

In this investigation, we extend the standard verification constraints discussed above. In particular, we do *not* assume that an exact solution exists, and we modify the error ansatz accordingly to allow calculation of oscillatory convergence. By oscillatory convergence, we are referring to the case where the computational solution approaches closer and closer to the exact solution as the zoning is refined, but sometimes with computational results of greater magnitude and sometimes with results of smaller magnitude than the exact solution. In addition, instead of solving the ansatz analytically, we solve it using Newton's method. A computational solution allows for a more complex ansatz, if desired. As a consequence of the solution method, one calculates a pointwise *estimation* of the "exact" solution that is mathematically consistent with the convergence parameters. Viewed alone, the modifications we propose are relatively minor (indeed, trivial) extensions of the standard approach. This approach may be particularly useful in situations that could contain large numbers of oscillatory converging points, such as phenomena containing discontinuities (e.g., shocks).

As part of this report, we seek to explore the accuracy of the estimated solution by applying the procedure to problems for which an exact solution does exist. This comparison provides quantitative—albeit limited—guidance as to how the simulation code may behave in the case in which an exact solution does not exist, examples of which we also examine. There are differences in the convergence rates calculated using an estimated solution and an exact solution. Understanding the difference between the estimated and exact solutions is therefore critical to understanding the error of convergence rates calculated without an exact solution.

---

[1] Another aspect of code verification is the Method of Manufactured Solutions [Sal00,Roa02, Knu03], which we do not discuss. There are additional elements of verification, related primarily to software issues (including, e.g., code coverage metrics). We limit our investigation to the "code physics verification." For extensive reviews of verification, see [AIAA98, IEEE98, Roa98a, Roa98b, Roa98c, Obe03, ASME04, Roy05].

[2] Note that *calculation verification* is distinct from *code comparison* [Tru03], which, as almost always practiced, is not part of verification per se.

The balance of this report is structured as follows. In §2, we review standard convergence analysis. This information forms the basis for the development in §3 of the extended convergence analysis that is the foundation of our work. We present results of this approach on a small set of gas dynamics problems in §4; these problems include both 1-D and 2-D Cartesian geometry problems, some having smooth solutions and others exhibiting discontinuities. We summarize this research and conclude in §5.

2. Standard Verification Convergence Analysis

Throughout this report we consider the evaluation of the numerically computed solution to partial differential equations that depend on both space $\boldsymbol{x}$ and time t. Although the applications we consider in §4 are restricted to the dynamics of a single, inviscid, non-heat-conducting, polytropic gas, the method we develop applies to numerical solutions of space- and time-dependent partial differential equations (PDE). We first restrict ourselves to the 1-D case, i.e., where there is only a single spatial variable. In this case, the standard error ansatz regarding the behavior of pointwise discretization error at position x and time t is given by [Kam02],

$$\xi^*(x,t) - \xi(x,t)_{\Delta x}^{\Delta t} = E_0(x,t) + A(x,t)(\Delta x)^{q(x,t)} + B(x,t)(\Delta t)^{r(x,t)} + o\left((\Delta x)^{q(x,t)},(\Delta t)^{r(x,t)}\right). \tag{2-1}$$

Because Eq. (2-1) has been written pointwise, all variables are functions of position and time. In this expression, ξ^* is the exact solution for some physical quantity such as density or pressure, and $\xi_{\Delta x}^{\Delta t}$ is the computed solution for the same physical quantity obtained on a grid with characteristic discrete spatial scale Δx and characteristic discrete time scale Δt. A fixed grid and time step are assumed with no spatial or temporal refinement as the simulation proceeds. The zeroth order error is designated E_0, q is the spatial convergence rate, r is the temporal convergence rate, and A and B are the corresponding convergence prefactors. The expression $o((\Delta x)^q,(\Delta t)^r)$ represents higher order terms that approach zero faster than $(\Delta x)^q$ and $(\Delta t)^r$ as both Δx and Δt become vanishingly small.

In the following development, all higher order terms are assumed small due to a small grid spacing and are neglected. Previous experience suggests that temporal errors are small compared to spatial errors, so the temporal errors are neglected as well. For the moment, we assume that the exact solution is unknown and one must solve for it. We refer to an exact solution that is calculated from the error ansatz as an estimated solution and designate it by $\hat{\xi}$. Rearranging the expression with all the unknowns on the right hand side and with the understanding that the computational value and all unknowns are functions of (x,t),

$$\xi_{\Delta x} = \hat{\xi} - E_0 - A(\Delta x)^q. \tag{2-2}$$

We assume consistency of the numerical method with the continuous equations and that it converges to the exact solution, in which case there is no zeroth order error. Eq. 2-2 then becomes

$$\xi_{\Delta x} = \hat{\xi} - A(\Delta x)^q. \tag{2-3}$$

When the estimated solution is calculated, it will effectively contain any zeroth order, temporal and all higher order error terms that have been neglected. The nature of the estimated solution is, therefore, a strong function of the error ansatz selected. The estimated solution in Eq. (2-3) will produce a value corresponding to the limit for the computational solution with infinitely small spatial zoning, but with a finite temporal discretization. Some spatial errors will persist through the higher order spatial terms that have been neglected. The estimated solution is *not* equivalent to an exact, analytical solution.

The error ansatz (2-3) is valid for any geometry in one dimension, but may also be used for two and three spatial dimensional problems. The only caveat to higher dimensions is that the ansatz is limited to Cartesian geometry with all of the discretizations along different dimensions equivalent. For mesh geometries that are not Cartesian, it may not be possible to have equal discretizations between the different dimensions. For example, in spherical geometry, $\Delta\theta$ is inherently different than Δr. With minor modification, the ansatz may be extended to other geometries in multiple dimensions or to discretization schemes without equivalent spacing.

With three unknowns, three calculations of different zoning completely specify a solution for the ansatz, with coarse (c), medium (m), and fine (f) zoning,

$$\xi_c = \hat{\xi} - A(\Delta x_c)^q, \qquad \xi_m = \hat{\xi} - A(\Delta x_m)^q, \qquad \xi_f = \hat{\xi} - A(\Delta x_f)^q. \tag{2-4}$$

In order to solve Eqs. (2-4), the calculated values are mapped onto the coarse grid by spatial averaging. Assuming that the zoning ratios (σ defined in Eq. 2-5 below) are the same,

$$\Delta x_c = \sigma \Delta x_m = \sigma^2 \Delta x_f, \tag{2-5}$$

and eliminating the estimated solution, Eqs. (2-4) become

$$\xi_m - \xi_c = A\Delta x_f^q \sigma^q (\sigma^q - 1), \qquad \xi_f - \xi_m = A\Delta x_f^q (\sigma^q - 1). \tag{2-6}$$

The solutions to Eqs. (2-6) are

$$q = \log\left(\frac{\xi_m - \xi_c}{\xi_f - \xi_m}\right) / \log(\sigma), \qquad A = \frac{\xi_f - \xi_m}{\Delta x_f^q (\sigma^q - 1)}, \qquad \hat{\xi} = \xi_f + A\Delta x_f^q (\sigma^q - 1). \tag{2-7}$$

The fundamental assumption of the ansatz is that error decreases as zone size decreases,

$$\left|\hat{\xi} - \xi_c\right| > \left|\hat{\xi} - \xi_m\right| > \left|\hat{\xi} - \xi_f\right| \geq 0. \tag{2-8}$$

At any point in the mesh, the order of the numerical values of the physical variables output by the simulation, ξ_c, ξ_m, and ξ_f, from largest to smallest, may be in one of six possible sequences. In the two cases where the coarse calculation value is intermediate,

$$\xi_m \geq \xi_c \geq \xi_f, \quad \text{or} \quad \xi_f \geq \xi_c \geq \xi_m, \tag{2-9}$$

then, there is no value for the estimated solution that satisfies Eqs. (2-8). In such cases, convergence may not be calculated for the cell.

If the simulation values are increasing with Δx such that

$$\xi_f < \xi_m < \xi_c, \tag{2-10}$$

then the ansatz (2-3) is valid and the solution space for the estimated solution in order to satisfy Eqs. (2-8) is

$$\hat{\xi} \leq \xi_f. \tag{2-11}$$

Likewise, if the simulation values are decreasing with Δx, then the ordering of the simulation values and the solution space for the estimated solution are respectively given by,

$$\xi_f > \xi_m > \xi_c, \qquad \hat{\xi} \geq \xi_f. \tag{2-12}$$

We refer to the previous two cases as monotonic convergence. Two possibilities remain, which represent oscillatory convergence. They and their solution spaces for the estimated solution are

$$\begin{aligned} &\xi_m > \xi_f > \xi_c, \qquad \frac{\xi_m + \xi_f}{2} > \hat{\xi} > \frac{\xi_m + \xi_c}{2}, \\ &\xi_c > \xi_f > \xi_m, \qquad \frac{\xi_m + \xi_f}{2} < \hat{\xi} < \frac{\xi_m + \xi_c}{2}. \end{aligned} \tag{2-13}$$

It is possible for all three computational points to reside outside the allowable solution space with oscillatory convergence. Although oscillatory convergence satisfies Eqs. (2-8), the standard ansatz does not allow it. When solving for q with oscillatory convergence, one finds the argument of the natural logarithm to be negative in Eqs. (2-7). Typically, only points with asymptotic convergence have been calculated. Most sets of points in the majority of simulations do not exhibit oscillatory convergence, so calculating monotonic convergence has proven an acceptable method for most problems. Unfortunately, oscillatory convergence may occur in some problems, e.g., at shock and discontinuity boundaries, and may therefore be important for non-smooth problems.

In addition to calculating pointwise convergence, global convergence rates may also be calculated using various global norms. The global norm ||•|| is a functional that maps its argument to the non-negative real numbers according to the definition [Hag88],

$$\|\mathrm{y}\|_\alpha \equiv \left(|y_1|^\alpha + |y_2|^\alpha + \ldots |y_N|^\alpha\right)^{1/\alpha}, \tag{2-14}$$

where **y** is some vector and α is an integer. The norm is effectively a measure of the length of the vector. In the case of simulations, the vector is the collection of values from each computational cell with a total of N cells on the coarse grid. Once the estimated solution has been determined, the norm for the computational error may be calculated,

$$\left\|\hat{\xi} - \xi_{\Delta x}\right\|_\alpha \equiv \left(\sum_{i=1}^{N} \left|\hat{\xi}(x_i,t_i) - \xi_{\Delta x}(x_i,t_i)\right|^\alpha\right)^{1/\alpha}. \tag{2-15}$$

The particular norm should appropriately account for the nature of the functions being quantified, e.g., the L_2 "energy" norm (α = 2) for smooth solutions and the L_1 "total variation" norm (α = 1) for discontinuous solutions. The equations for global convergence may be written,

$$\left\|\hat{\xi} - \xi_c\right\|_\alpha = A_g \Delta x_c^{q_g}, \qquad \left\|\hat{\xi} - \xi_f\right\|_\alpha = A_g \Delta x_f^{q_g}. \tag{2-16}$$

The g subscript on the convergence rate and prefactor is a reminder that they represent global values and are functions of time, but not of space. Taking σ to be the ratio between the coarse and fine zoning, the solutions to Eqs. (2-16) are,

$$\begin{aligned} q_g &= \left[\log\left\|\hat{\xi} - \xi_c\right\|_\alpha - \log\left\|\hat{\xi} - \xi_f\right\|_\alpha\right] \Big/ \log(\sigma), \\ A_g &= \left\|\hat{\xi} - \xi_c\right\|_\alpha \Big/ \left(\Delta x_c\right)^{q_g}. \end{aligned} \tag{2-17}$$

Now we consider the pointwise case when the exact solution is known. Only two computational solutions are required to solve for convergence and the *pointwise* convergence relations become,

$$\xi^* - \xi_c = A \Delta x_c^q, \qquad \xi^* - \xi_f = A \Delta x_f^q, \tag{2-18}$$

where the exact and calculated solutions, A and q are all functions of position and time. Rigorously, the exact solution at the center of the computational cell should not be used for codes that employ the finite volume method instead of finite difference schemes, as does the RAGE code used in this study. Instead, the integrated average of the exact solution over the entire cell should be used in Eq. (2-18). However, previous has shown little difference in the results between convergence calculations that used the exact solution at the zone center and calculations using the integral of the exact solution across the zone.

Although the exact solution may be calculated on the same grid as the fine computational solution, we instead map the fine solution onto the coarse grid instead because the convergence constant and rate are both spatially discretized on the coarse grid. The solutions to Eqs. (2-10) are,

$$\begin{aligned} q &= \left[\log\left(\xi^* - \xi_c\right) - \log\left(\xi^* - \xi_f\right)\right] \Big/ \log(\sigma) , \\ A &= \left(\xi^* - \xi_c\right) \Big/ \left(\Delta x_c\right)^q . \end{aligned} \tag{2-19}$$

The equations for global convergence and their solutions with a known exact solution are analogous to the global case with the estimated solution, Eqs. (2-16) and (2-17), only the estimated solution is replaced by the exact solution. When calculating the norms with known exact solutions, one may use either the fine grid solutions interpolated onto the coarse grid, or the exact solution expanded to the fine grid.

3. Extended Verification Convergence Analysis

The ability to calculate oscillatory convergence may be important in determining global convergence of the algorithm. In order to do this, the error ansatz (2-3) and related Eqs. (2-4) need only be changed slightly by considering absolute values of the difference terms, *i.e.*,

$$\left|\hat{\xi} - \xi_c\right| = A\left(\Delta x_c\right)^q, \qquad \left|\hat{\xi} - \xi_m\right| = A\left(\Delta x_m\right)^q, \qquad \left|\hat{\xi} - \xi_f\right| = A\left(\Delta x_f\right)^q . \tag{3-1}$$

These equations can no longer be solved analytically. Instead, Newton's method can be employed to computationally solve for the estimated solution, A, and q simultaneously [Pre92a]. An advantage of Newton's method is that it allows for the solution of a more complex ansatz than Eqs. (2-3), if desired. The equations to be solved are rewritten,

$$\boldsymbol{F} = \begin{bmatrix} F_1 \\ F_2 \\ F_3 \end{bmatrix} = \begin{bmatrix} \left|\hat{\xi} - \xi_c\right| - A\left(\Delta x_c\right)^q \\ \left|\hat{\xi} - \xi_m\right| - A\left(\Delta x_m\right)^q \\ \left|\hat{\xi} - \xi_f\right| - A\left(\Delta x_f\right)^q \end{bmatrix}, \tag{3-2}$$

in which $\boldsymbol{F}$, $\hat{\xi}$, A, and q change with each iteration of the Newton solver. The objective is to determine the variables such that $\boldsymbol{F} = 0$, within some tolerance, for all $\boldsymbol{F}$. Implicit in Eq. (3-2) is the assumption that values are in an asymptotic regime consistent with the error ansatz, so that higher-order terms can justifiably be neglected. All quantities in Eq. (3-2) are to be evaluated on the coarse grid, so that the medium and fine computational solutions must be spatially averaged.

A vector of the three unknowns is defined,

$$\boldsymbol{b}_j \equiv \begin{bmatrix} b_1 \\ b_2 \\ b_3 \end{bmatrix} = \begin{bmatrix} \hat{\xi} \\ A \\ q \end{bmatrix}, \tag{3-3}$$

and the Jacobian matrix of Eq. (3-2),

$$\boldsymbol{J} \equiv \frac{\partial F_i}{\partial b_j}, \qquad \frac{\partial F_i}{\partial b_1} = \begin{cases} +1, \ if \ \left(b_1 - \xi_i\right) > 0 , \\ 0, \ if \ \left(b_1 - \xi_i\right) = 0 , \\ -1, \ if \ \left(b_1 - \xi_i\right) < 0 , \end{cases} \qquad \begin{aligned} \frac{\partial F_i}{\partial b_2} &= -\Delta x_i^q , \\ \frac{\partial F_i}{\partial b_3} &= -A\Delta x_i^q \ln\left(\Delta x_i\right). \end{aligned} \tag{3-4}$$

Although the derivative of the argument of the absolute value is technically undefined when its argument is zero, it appeared reasonable to set it to zero for such a special case. An analytical Jacobian was used for the work presented here, but a subroutine was inserted into the code in order to computationally determine the Jacobian for a more complex ansatz.

In order to solve for the change in $\boldsymbol{b}$ in order for $\boldsymbol{F} = 0$, the Jacobian matrix is multiplied by the change in each variable and then equated with the negative of the vector $\boldsymbol{F}$,

$$\boldsymbol{J} \bullet \delta\boldsymbol{b} = -\boldsymbol{F} \tag{3-5}$$

To solve Eq. (3-5) for $\boldsymbol{\delta b}$, the Jacobian matrix is factored into lower, $\boldsymbol{L}$, and upper, $\boldsymbol{U}$ triangular matrices using partial pivoting. The following two equations are then solved using a combination of forward and backward substitution:

$$\boldsymbol{L} \bullet \boldsymbol{y} = -\boldsymbol{F}, \qquad \boldsymbol{U} \bullet \delta\boldsymbol{b} = \boldsymbol{y}. \tag{3-6}$$

Taking the full Newton step was found to be inadvisable. Implementation of the Newton solver using the full Newton step resulted in few points converging. The direction of the vector $\delta\boldsymbol{b}$ is guaranteed to be a decent direction for $\boldsymbol{F}$, but only at the starting point (at $\boldsymbol{b}$). Nonlinear effects can quickly result in an increase (or larger than linear decrease) of $\boldsymbol{F}$ as one travels along the vector $\delta\boldsymbol{b}$. A method had to be implemented in order to determine the appropriate distance along $\delta\boldsymbol{b}$ to travel and take the iterative step [Pre92b]. To do so, a metric of what defines an acceptable step is needed. The functions f and g are defined,

$$f \equiv \frac{1}{2}\boldsymbol{F} \bullet \boldsymbol{F}, \qquad g(\lambda) \equiv f\left(\boldsymbol{b}_{old} + \lambda\delta\boldsymbol{b}\right), \qquad \frac{dg(\lambda)}{d\lambda} = \nabla f \bullet \delta\boldsymbol{b}. \tag{3-7}$$

Calculating the minimization of the function g would waste too much computational effort. The function g should not be minimized, rather simply finding a step that produces an acceptable decrease in f is needed. An acceptable decrease is defined as one for which

$$g(\lambda) \le g(0) + \alpha\left(\lambda \frac{dg(0)}{d\lambda}\right), \tag{3-8}$$

in which α is chosen to be about 10^{-4}. Thus, we do not seek the entire decrease predicted from first order, but accept a smaller decrease if the nonlinear terms are significant.

The full Newton step ($\lambda = 1$) is tried first [Pres92b]. If it is unsuccessful, then the function g is modelled using a second order polynomial fit to the three known points, $g(1)$, $dg(1)/d\lambda$, and $g(0)$. The parabola was minimized by setting the derivative to zero and solving for λ. The parabola should have a positive coefficient for the squared term resulting in the extrema being a minimum. If the second value of λ is unacceptable, a cubic polynomial fit is used and minimized. The procedure is repeated until an acceptable step length is found. One must be careful not to make the step too short. A minimum step size was prescribed. In addition to requiring that $\boldsymbol{F} = 0$ within some tolerance for convergence to be declared, the code also required that $\delta\boldsymbol{b}$ be reduced to some minimum tolerance as well. The procedure for finding the appropriate step length is not as related to bisection as to function approximation. Frequently bisection is used as a backup to Newton's method, but unfortunately in multidimensional parameter space, this is not possible in our problem.

A related consideration in calculating an appropriate step length is the validity of the Newton method. Newton iteration assumes dominance of the first order terms. Steps large enough to produce second order terms that are of significant size compared to the first order terms must be avoided. In Eqs. (3-2), there are two second-order terms that are nonzero,

$$\frac{\partial^2 F_i}{\partial q^2}(\delta q)^2 = -A\left[\ln(\Delta x_i)\right]^2 \Delta x^q (\delta q)^2, \qquad \frac{\partial^2 F_i}{\partial A \partial q}(\delta A \delta q) = -\ln(\Delta x)\Delta x^q (\delta A \delta q). \tag{3-9}$$

By taking the ratio of second to first derivatives, the expressions for maximum step sizes may be determined,

$$\delta q << \frac{1}{\ln(\Delta x_f)}, \qquad \delta A << A. \tag{3-10}$$

Assignment of an appropriate initial value for the array of unknowns to be used in the iterative solver is important. If the fine grid computational solution was within the allowable solution space for the estimated solution, then the starting point for the estimated solution was chosen to be the fine grid solution,

$$b_1^{(0)} = \hat{\xi}^{(0)} = \xi_f \ , \tag{3-11}$$

where the superscript indicates the iteration index. With this assignment, we obtain initial values for the other two unknowns, which provide solutions for the convergence rate q and prefactor A in the case where an exact solution is given:

$$\begin{aligned} b_2^{(0)} &= A^{(0)} = \left| b_1^{(0)} - \xi_c \right| \Big/ \left(\Delta x_c \right)^{q^{(0)}}, \\ b_3^{(0)} &= q_i^{(0)} = \left[\log\left| b_1^{(0)} - \xi_c \right| - \log\left| b_1^{(0)} - \xi_m \right| \right] \Big/ \log\sigma. \end{aligned} \tag{3-12}$$

If the fine grid solution was not within the acceptable solution space for the estimated solution, then starting at the fine grid solution did not always yield convergence. Instead, the estimated solution was estimated by calculating the center of the solution space defined by Eqs. (2-13),

$$b_1^{(0)} = \hat{\xi}^{(0)} = \frac{1}{4}\left(\xi_c + 2\xi_m + \xi_f \right). \tag{3-13}$$

The associated pointwise convergence rate and prefactor were then determined according to Eqs. (2-7) for each cell. A loop was placed over all cells in the mesh so that pointwise convergence was calculated for each cell.

Although most grid points converged, a few did not for a variety of reasons. First, at certain points the ordering of the function values was inconsistent with the assumption of the ansatz as described by Eqs. (2-8). Second, non-convergence follows if all of the function values are essentially equal, to within a user-specified tolerance. Third, the Newton method sometimes produced a zero element on the diagonal of the upper triangular matrix, which would give a divide by zero error in the code. Most of the time, this could be overcome by simply assigning a minimum value to all the diagonal elements, but the price of such a procedure was to eliminate the certainty that $\delta\boldsymbol{b}$ was indeed a descent direction for f. If $\delta\boldsymbol{b}$ was an ascent direction, then convergence could not be calculated. The last and least common reason for points not converging was that there was an insufficient number of iterations of the Newton solver. The maximum number of iterations was set to 100. If the solver failed to converge on a few points in a particular problem, a reduction in the tolerance of the convergence criteria was made until all points either converged or didn't in under 100 Newton iterations. Experimentation with code parameters showed that increasing the maximum number of Newton solver iterations did not usually result in all the points converging, while lowering the tolerance did. The mesh points at which convergence was not obtained were flagged and treated specially in the subsequent analysis. As a related comment, sometimes the fine grid computational solution was within machine precision of the exact analytical solution, in which case the convergence rate and constant could not be calculated for the exact solution.

Upon completion of the analysis for a given problem, one obtains the set of parameters $\{\hat{\xi}_i, A_i, q_i\}$ at the (coarse) grid points of the computational mesh. As with any set of data, one can evaluate the statistical measures of these quantities; the simplest statistics to evaluate are the sample mean and standard deviation (i.e., the square root of the variance)

of the convergence rates $\{q_i\}$ and prefactors $\{A_i\}$. As noted above, there are found to be grid points for which a converged solution was not obtained; these points were excluded from the evaluation of the mean and standard deviation. More precisely, for the case of the convergence rate, we evaluate the mean $\hat{q}_i$ and variance $\hat{\sigma}^2_{q_i}$ as:

$$\hat{q}_i = \frac{1}{N'}\sum_{i=1}^{N'} q_i \quad \text{and} \quad \hat{\sigma}^2_{q_i} = \frac{1}{N'-1}\sum_{i=1}^{N'}\left(q_i - \hat{q}_i\right)^2 , \tag{3-14}$$

where N' is the total number of "valid" grid points, i.e., points for which a converged solution was obtained. An identical procedure is followed for the statistical characterization of the convergence prefactor via $\hat{A}_i$ and $\hat{\sigma}^2_{A_i}$. One could develop a more thorough statistical characterization of the approximate probability distribution function of these data, but we have not pursued such an analysis in this report.

To summarize, the approach we have presented allows for the evaluation of the local asymptotic convergence parameters together with an estimate of the function value at each (coarse) grid point. These numerical estimates are obtained as the solution to a set of nonlinear, coupled equations. This process provides estimates for the solution and, through the convergence parameters, the associated discretization error at each point for problems that do not possess exact solutions. We now turn to demonstrations of this method.

4. Results and Interpretation

In this section, we apply the technique described above to a set of hydrodynamics problems. The governing equations for these problems are the Eulerian-frame equations for the dynamics of a single, inviscid, non-heat-conducting gas, describing the conservation of mass, momentum, and total energy as:

$$\begin{aligned}
&\frac{\partial \rho}{\partial t} + \frac{\partial}{\partial x}\left(\rho u_x\right) + \frac{\partial}{\partial y}\left(\rho u_y\right) = 0 , \\
&\frac{\partial\left(\rho u_x\right)}{\partial t} + \frac{\partial}{\partial x}\left(\rho u_x^2 + p\right) + \frac{\partial}{\partial y}\left(\rho u_x u_y\right) = 0 , \\
&\frac{\partial\left(\rho u_y\right)}{\partial t} + \frac{\partial}{\partial x}\left(\rho u_x u_y\right) + \frac{\partial}{\partial y}\left(\rho u_y^2 + p\right) = 0 , \\
&\frac{\partial\left(\rho E\right)}{\partial t} + \frac{\partial}{\partial x}\left[\rho u_x\left(E + \frac{p}{\rho}\right)\right] + \frac{\partial}{\partial y}\left[\rho u_y\left(E + \frac{p}{\rho}\right)\right] = 0 .
\end{aligned} \tag{4-1}$$

In these equations, ρ is the density, u_x is the x-velocity, p is the thermodynamic pressure, and $E = (1/2)\left(u_x^2 + u_y^2\right) + e$ is the specific total energy, where e is the specific internal energy (SIE). We assume the polytropic gas equation of state (EOS)

$$p = (\gamma - 1)\ \rho\ e , \tag{4-2}$$

where γ is the adiabatic exponent. We consider the following four problems:

1. a 2-D linear acoustic wave problem;
2. a 2-D nonlinear acoustic wave problem;
3. a 1-D Riemann problem (i.e., a shock-tube problem); and
4. a 2-D Riemann problem.

We present a matrix of characterizations for these problems in Table 1. We have chosen this set of problems as it offers a mixture of solution properties that spans the issues of smooth and discontinuous solution behavior, either with or without an exact solution. In particular, problems 1 and 3 have exact solutions; therefore, for these problems we can compare the outcome of our analysis, which provides an estimate of the exact solution, with the true solution. Problems 2 and 4 do not have exact solutions, however, so the results of our analysis will provide new answers in addition to convergence characteristics.

Table 1. Features of problems considered in this report.

	Does possess an exact solution	*Does not possess an exact solution*
Smooth solution	1: 2-D linear acoustic wave	2: 2-D nonlinear acoustic wave
Non-smooth solution	3: 1-D Riemann problem	4: 2-D Riemann problem

We used the RAGE hydrodynamics code to perform the numerical simulations. RAGE is an adaptive mesh refinement (AMR) hydrodynamics code that uses a high-order Godunov (direct Eulerian, piecwise linear) method with an approximate Riemann solver to obtain the solution of the gas dynamics equations. We only consider 1-D and 2-D Cartesian geometries in the problems that we evaluate. The calculations that we perform with RAGE were all done on uniform, non-AMR grids; we restrict the calculations considered in this manner to be consistent with the error ansatz that governs these analyses. Also, wherever possible we use the default input parameters to the code; of coarse, we modify the input parameters required to assign the initial conditions, the computational mesh, and the output data, which were specified in NCSA-compliant HDF files [NCSa, NCSb].

All simulations were run with constant, forced, time steps. The same time step was used for meshes with different zonings on the same problem. Simulations without forced time step were run first, in order to determine what the appropriate size of the forced time step should be.

Four physical quantities were calculated and analyzed for each problem. They were density, pressure, SIE, and either speed or x-velocity (for the 1D test problem). Four simulations of different zoning were run for each test problem, a total of sixteen runs in all. As the convergence code requires three simulations of different zoning to perform an analysis, this resulted in two convergence calculations for each variable and each problem, or

eight convergence calculations total. We now turn to descriptions and evaluation of the test problems.

4a. A 2-D linear acoustic wave problem

The 2-D acoustic wave problem, described in detail in [Kam03] (see also [Lan87, Whi74]), is based on specific initial condition for the 2-D Cartesian gas dynamics equations. When the amplitude of the initial conditions is sufficiently small (in a manner to be made precise), then there exists a closed form solution that is asymptotically valid for early time. This closed form result involves the solution of a linear wave equation, so we refer to this configuration as the "linear" acoustic wave problem, which we analyze in this section. For initial conditions of the same form but with larger initial amplitude, the duration of simulation time for which asymptotic solution is valid decreases, and there is no closed-form solution for the resulting nonlinear problem at the same final time. In the subsequent section, we consider the latter case, which we refer to as the "nonlinear" acoustic wave problem. The initial conditions for both of these Cartesian geometry problems consist of constant, uniform values of density, pressure, and velocity that have given sinusoidal perturbations. For the linear problem, the initial amplitude of these perturbations is sufficiently small that the true solution oscillates as a acoustic wave solution of a linear wave equation for relatively long times. In the nonlinear problem, the initial amplitude of the perturbations is large, so that nonlinearities develop more quickly and no asymptotically exact solution is available at the times of interest. In either case, however, the solution remains smooth for the times considered.

To further motivate the solution to these 2-D acoustic problems, we posit that the solution at all times consists of a sum of uniform, constant physical fields, subscripted 0, and small (in a sense to be made precise) perturbations, indicated by primes:

$$\begin{aligned} \rho &= \rho_0 + \rho' , \\ p &= p_0 + p' , \\ (u_x, u_x) &= (u_{x0}, u_{y0}) + (u_x', u_y') , \end{aligned} \tag{4-3}$$

for the density ρ, pressure p, and x- and y-velocities (u_x, u_y). For the polytropic gas EOS, the square of the quiescent sound speed, c_0, can be expressed as:

$$c_0^2 = \gamma (\gamma - 1) e_0 . \tag{4-4}$$

The ordering of the terms in Eqs. (4-3) is based on the primed terms being small in the following quantitative sense:

$$\rho'/\rho_0 << 1, \quad p'/p_0 << 1, \quad u_x'/c_0, \quad u_y'/c_0 << 1 . \tag{4-5}$$

As shown in [Lan87, Whi74], the solution for the primed quantities can be derived from a potential $\varphi(\boldsymbol{x},t)$ that satisfies the following linear wave equation:

$$\frac{\partial^2 \varphi}{\partial t^2} - c_0^2 \nabla^2 \varphi = 0 , \tag{4-6}$$

The velocity perturbation is given by the gradient of this potential:

$$\left(u_x', u_y'\right) = \nabla\varphi = \left(\frac{\partial\varphi}{\partial x}, \frac{\partial\varphi}{\partial y}\right), \tag{4-7}$$

while the pressure and density perturbations are related to the time derivative of the potential:

$$\rho' = -\frac{\rho_0}{c_0^2}\frac{\partial\varphi}{\partial t}, \qquad p' = -\rho_0\frac{\partial\varphi}{\partial t}. \tag{4-8}$$

The problem we consider is defined on the unit square $\Omega \equiv \{(x,y):(x,y)\in[0,1]\times[0,1]\}$ with periodic boundary conditions along the edge $\partial\Omega$. We prescribe the temporal dependence to be oscillatory with angular frequency ω. In this case, the solution for the potential is

$$\varphi(\boldsymbol{x},t) = \frac{\varepsilon}{|\boldsymbol{k}|}\sin(\boldsymbol{k}\cdot\boldsymbol{x})\cos(\omega t), \tag{4-9}$$

where the wavevector $\boldsymbol{k} \equiv k_x\hat{x} + k_y\hat{y}$ governs both the direction and period of the spatial variation of the solution, where $\hat{x}$ and $\hat{y}$ are unit vectors. Based on these relations, the closed-form solution for the specific problem we consider is given in Table 2. The initial conditions (IC) are a special case of this solution and are given in Table 3.

Table 2. 2-D linear acoustic wave solution.

Variable	*Base solution* $(\bullet)_0$	*Perturbed solution* $(\bullet)'$
u_x	0	$\varepsilon\,(k_x/k)\cos(k_x x + k_y y)\cos(\omega t)$
u_y	0	$\varepsilon\,(k_y/k)\cos(k_x x + k_y y)\cos(\omega t)$
ρ	1	$\varepsilon\,(\rho_0\omega/k)\sin(k_x x + k_y y)\sin(\omega t)$
p	3/10	$(\varepsilon/c_0^2)\,(\rho_0\omega/k)\sin(k_x x + k_y y)\sin(\omega t)$

Table 3. 2-D linear acoustic wave initial conditions.

Variable	*Base IC* $(\bullet)_0$	*Perturbed IC* $(\bullet)'$
u_x	0	$\varepsilon\,(k_x/k)\cos(k_x x + k_y y)$
u_y	0	$\varepsilon\,(k_y/k)\cos(k_x x + k_y y)$
ρ	1	0
p	3/10	0

In the expressions in this table, k represents the magnitude of the wavevector, i.e., $|\boldsymbol{k}|$. The specific parameters used in the problem we consider are given in Table 4.

Table 4. 2-D linear acoustic wave initial parameters.

γ	k_x	k_y	ω	ε
5/3	2π	2π	2π	10^{-4}

With these parameters, the calculation was run from an initial time of $t = 0$ s to a final time of $t = 0.2$ s on meshes containing 50×50, 100×100, 200×200, and 400×400 zones on the unit square.

We had to modify the RAGE initialization routine to assign the initial condition for the linear and nonlinear acoustic problems; these modifications were done to code version 2004-1126, yielding a version that we denote RAGE 2004-1126*. For the 1D and 2D Riemann problems, the standard version of RAGE, 2004-1126 was used.

The global convergence results are summarized in Tables 5–8. Table 5 contains the L_1 norm of the difference between the true exact solution and the computed solution over the various computational meshes. The purpose of showing the norms is not to provide information on the level of computational error, rather to show how the error changes and the code converges as a function of zoning. The values in this table can be used to compute the exact, pair-wise convergence rate q and convergence prefactor A for these results. Those values are compiled in Tables 6 and 7.

Table 5 shows a decrease in the global error of all physical quantities with zone size, as one would expect. Note that speed in the tables

$$u = \sqrt{u_x^2 + u_y^2} \tag{4-10}$$

is a scalar quantity, not a vector. Table 6 shows a decrease in the convergence rate with resolution, except for speed, which increases, then decreases again. Likewise, all of the prefactor values shown in Table 7 exhibit a decrease with zone size, except speed. Why the speed convergence rate and prefactor behave in this manner is unknown. Likewise, in Tables 6 and 7, the convergence rates and prefactors for the finest zoning for all quantities other than the speed are extremely small. We are uncertain as to why.

Global Convergence Results

Table 5. 2-D linear acoustic wave exact-computed L_1 errors at $t = 0.2$ s.

N_x, N_y	$\Delta x, \Delta y$ (cm)	$\left\|\rho^* - \rho_{\Delta x}\right\|_1$ (g cm^{-3})	$\left\|p^* - p_{\Delta x}\right\|_1$ (dyne cm^{-2})	$\left\|e^* - e_{\Delta x}\right\|_1$ (erg g^{-1})	$\left\|u^* - u_{\Delta x}\right\|_1$ (cm s^{-1})
50	0.02	2.81×10^{-7}	1.40×10^{-7}	8.43×10^{-8}	2.65×10^{-7}
100	0.01	6.61×10^{-8}	3.31×10^{-8}	1.99×10^{-8}	7.95×10^{-8}
200	0.005	1.62×10^{-8}	8.38×10^{-9}	5.48×10^{-9}	2.02×10^{-8}
400	0.0025	7.48×10^{-9}	4.70×10^{-9}	3.88×10^{-9}	5.68×10^{-9}

*RAGE version 2004-1126**

Table 6. 2-D linear acoustic wave exact convergence rate q at $t = 0.2$ s.

Range of cells	*Density*	*Pressure*	*Energy*	*Speed*
50,100	2.09	2.08	2.08	1.73
100,200	2.03	1.98	1.86	1.98
200,400	1.11	0.833	0.496	1.83

*RAGE version 2004-1126**

Table 7. 2-D linear acoustic wave exact convergence prefactor A at $t = 0.2$ s.

Range of cells	*Density*	*Pressure*	*Energy*	*Speed*
50,100	9.89×10^{-4}	4.89×10^{-4}	2.89×10^{-4}	2.34×10^{-4}
100,200	7.61×10^{-4}	3.08×10^{-4}	1.06×10^{-4}	7.15×10^{-4}
200,400	5.94×10^{-6}	6.93×10^{-7}	7.59×10^{-8}	3.29×10^{-4}

*RAGE version 2004-1126**

The first two rows in Table 5 are to be compared to the values in Table 8 (both shown in Figure 2), which are the L_1 norm of the difference between the exact solution and the estimated solution inferred on the indicated meshes (recall that three different meshes are required to infer an estimated solution on the coarsest mesh). Comparing the values in these two tables demonstrates that the estimated solution error is less than the computed solution error for the same grid, but more than the computed solution error for the fine grid. The estimated solution itself is a function of zone size and its corresponding error consistently drops with the zone size.

Table 8. 2-D linear acoustic wave exact-estimated solution error at t=0.2 s.

N_x, N_y	$\Delta x, \Delta y$ (cm)	$\left\|\rho^* - \hat{\rho}\right\|_1$ (g cm^{-3})	$\left\|p^* - \hat{p}\right\|_1$ (dyne cm^{-2})	$\left\|e^* - \hat{e}\right\|_1$ (erg g^{-1})	$\left\|u^* - u_{\Delta x}\right\|_1$ (cm s^{-1})
50 (100, 200)	0.02	1.25×10^{-7}	6.27×10^{-8}	3.76×10^{-8}	5.21×10^{-8}
100 (200, 400)	0.01	3.12×10^{-8}	1.56×10^{-8}	9.37×10^{-9}	2.27×10^{-8}

*RAGE version 2004-1126**

The mean and standard deviation of the computed pointwise convergence rate q over the computational mesh is shown in Table 9 and Figure 3, while Table 10 contains the corresponding inferred convergence prefactor A. Recall that these values are calculated using only those mesh points for which a convergence rate is obtained, which, for these calculations, was the entire mesh.

In all cases in Tables 9 and 10, the convergence rate and prefactor increase with a decrease in zone size, which is the opposite behavior observed from the global quantities. If the difference in computational results from two mesh resolutions is small, then likewise, the convergence rate and prefactor will be small. If there is a large difference in the com-

putational results from the same two mesh resolutions, then the large change is interpreted as a larger convergence rate and prefactor. One would expect as a simulation begins to converge and changes in the results with increased zoning decrease, then the convergence rate and prefactor will also decrease. Such behavior is observed in the global values.

One possible explanation for the increase in the convergence quantities with zoning is that there may be a few points that changed dramatically as the zoning was decreased producing relatively large convergence values, while most points produced a decrease in the convergence values. This hypothesis is supported by the large increase in the standard deviation going from the coarse to fine values.

Mean, Pointwise Convergence Results

Table 9. 2-D linear acoustic wave estimated convergence rate q at $t = 0.2$ s.

Range of cells	*Density*	*Pressure*	*Energy*	*Speed*
50 (100, 200)	2.60±0.290	2.60±0.291	2.60±0.292	2.45±0.120
100 (200, 400)	2.83±0.585	2.83±0.585	2.83±0.585	2.55±0.168

*RAGE version 2004-1126**

Table 10. 2-D linear acoustic wave estimated convergence coefficient A at $t = 0.2$ s.

Range of cells	*Density*	*Pressure*	*Energy*	*Speed*
50 (100, 200)	$(8.81\pm14.5)\times10^{-3}$	$(4.40\pm7.24)\times10^{-3}$	$(2.64\pm4.34)\times10^{-3}$	$(3.47\pm2.36)\times10^{-3}$
100 (200, 400)	$(1.48\pm5.32)\times10^{0}$	$(7.40\pm26.6)\times10^{-1}$	$(4.44\pm16.0)\times10^{-1}$	$(7.04\pm4.33)\times10^{-3}$

*RAGE version 2004-1126**

Figures 1a-d contain plots that further elucidate the results. Figures 1a–d contain plots of the estimated solution and difference between the estimated and exact solutions for the density, pressure, speed, and SIE at the final time on the two meshes for which estimated solutions are obtained. The sinusoidal nature of the solution is clearly evident in these images. For each of these physical quantities, the absolute magnitudes of the difference data are several orders of magnitude smaller than the corresponding computed or exact values. Also, the features of the differences are aligned with the solution structure.

Figure 2 contains plots of the L_1 norm of the difference between the computed solution and the true exact solution (i.e., the data in Table 5, in **black**) and the difference between the estimated solution and the true exact solution (i.e., the data in Table 8, in blue) as a function of the mesh size, for all quantities.

Figure 3 contains plots of the mean convergence rate q on the two computational meshes for which the estimated solution was obtained, for all physical quantities (i.e., the data in Table 9). These plots have uncertainty bounds indicating ± one standard deviation in these values, which are calculated from the distribution of convergence rate values on the mesh. The increase in standard deviation with decreasing zone size is clearly evident.

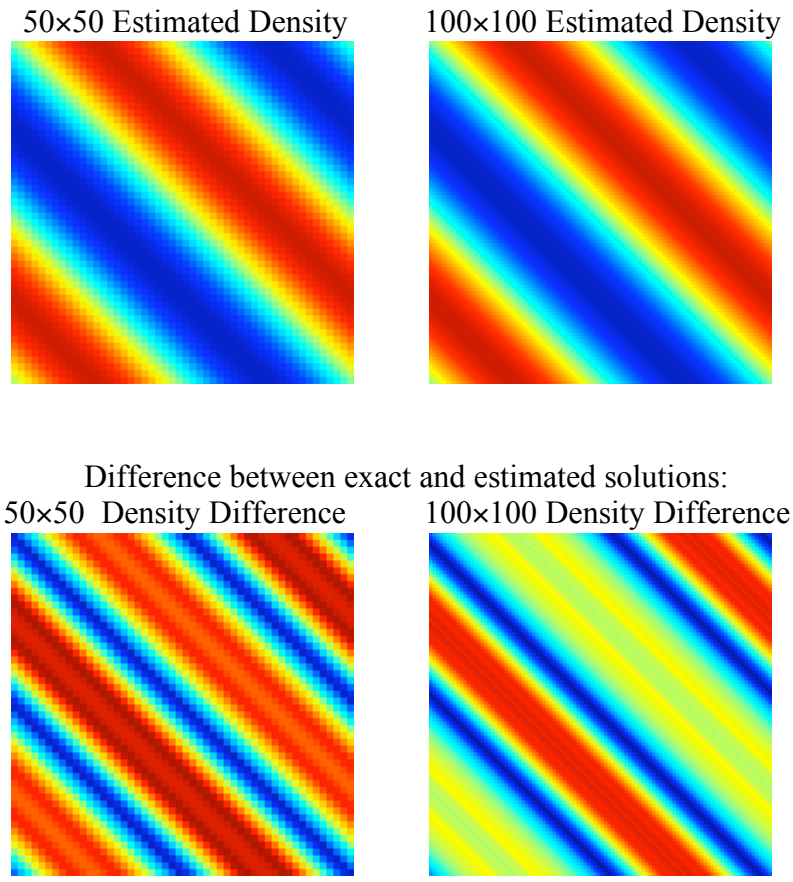

Figure 1a. Plots of the estimated density (top) and difference between estimated and exact density (bottom) for the 2-D linear acoustic wave problem at time $t = 0.2$ s on the two computational meshes considered. The left column has the results on the 50×50 mesh, the right column has results on the 100×100 mesh, both on the unit square. The density data (top row) range is (dark blue) $0.99985 \le \rho \le 1.00015$ (dark red); recall that $\rho \equiv 1.0$ uniformly at $t = 0$ and evolves into a sinusoidal wave with small perturbations around the initial condition. The density difference data (bottom row) range is (dark blue) $0.0 \le \Delta\rho \le$ {50: 2×10^{-7}; 100: 6×10^{-8}} (dark red). All values are in g/cm^3. *The estimated solution is extremely close to the exact solution for this problem*.

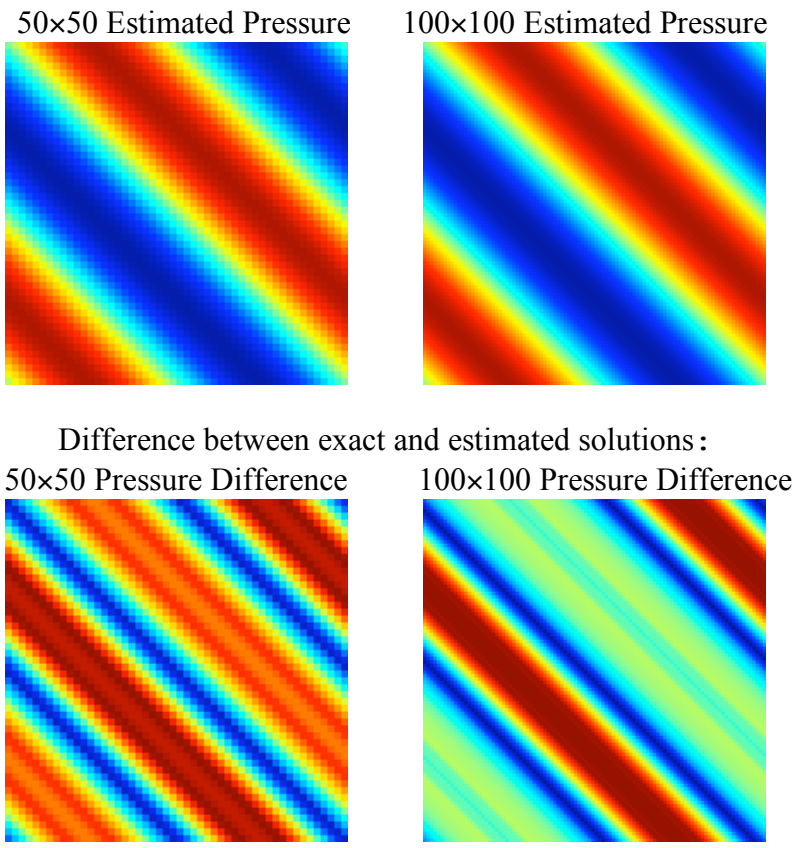

Figure 1b. Plots of the estimated pressure (top) and difference between estimated and exact pressure (bottom) for the 2-D linear acoustic wave problem at time $t = 0.2$ s on the two computational meshes considered. The left column has the results on the 50×50 mesh, the right column has results on the 100×100 mesh, both on the unit square. The pressure data (top row) range is (dark blue) $0.99985 \le p \le 1.00015$ (dark red). Recall that $p \equiv 0.3$ uniformly at $t = 0$ and evolves into a sinusoidal wave with small perturbations around the initial condition. The pressure difference data (bottom row) range is (dark blue) $0.0 \le \Delta p \le \{50: 1\times10^{-7};\quad 100: 3\times10^{-8}\}$ (dark red). All values are in dyne/cm^2. *The estimated solution is extremely close to the exact solution for this problem*.

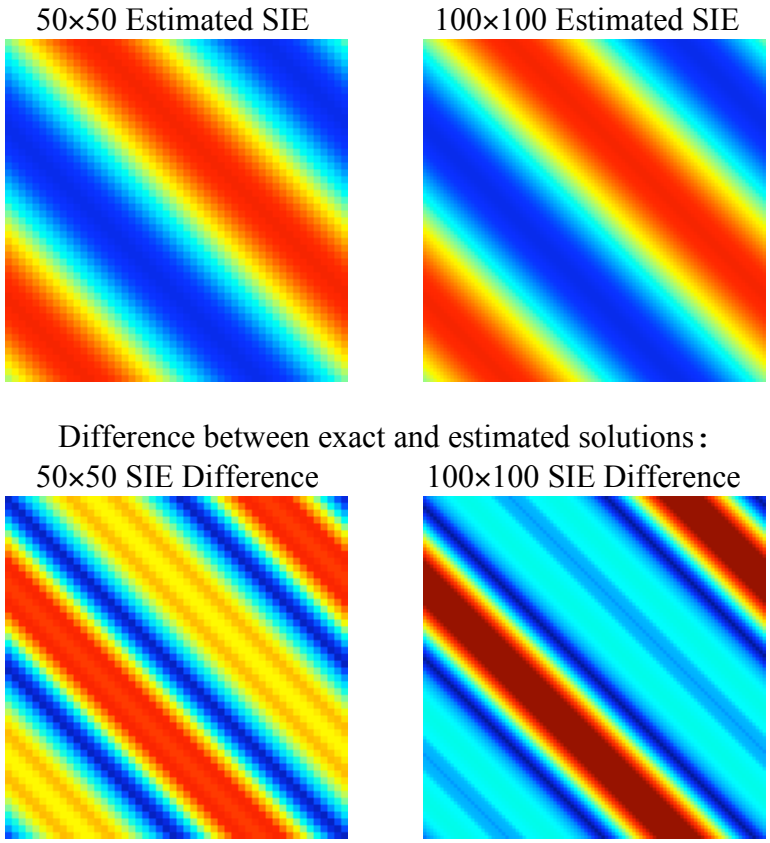

Figure 1c. Plots of the estimated SIE (top) and difference between estimated and exact SIE (bottom) for the 2-D linear acoustic wave problem at time $t = 0.2$ s on the two computational meshes considered. The left column has the results on the 50×50 mesh, the right column has results on 100×100 mesh, both on the unit square. The SIE data (top row) range is (dark blue) $0.44995 \leq e \leq 0.45005$ (dark red). Recall that $e \equiv 9/20$ uniformly at $t = 0$ and evolves into a sinusoidal wave with small perturbations around the initial condition. The SIE difference data (bottom row) range is (dark blue) $0.0 \leq \Delta e \leq \{50: 7\times10^{-8}; 100: 2\times10^{-8}\}$ (dark red). All values are in erg/g. *The estimated solution is extremely close to the exact solution for this problem*.

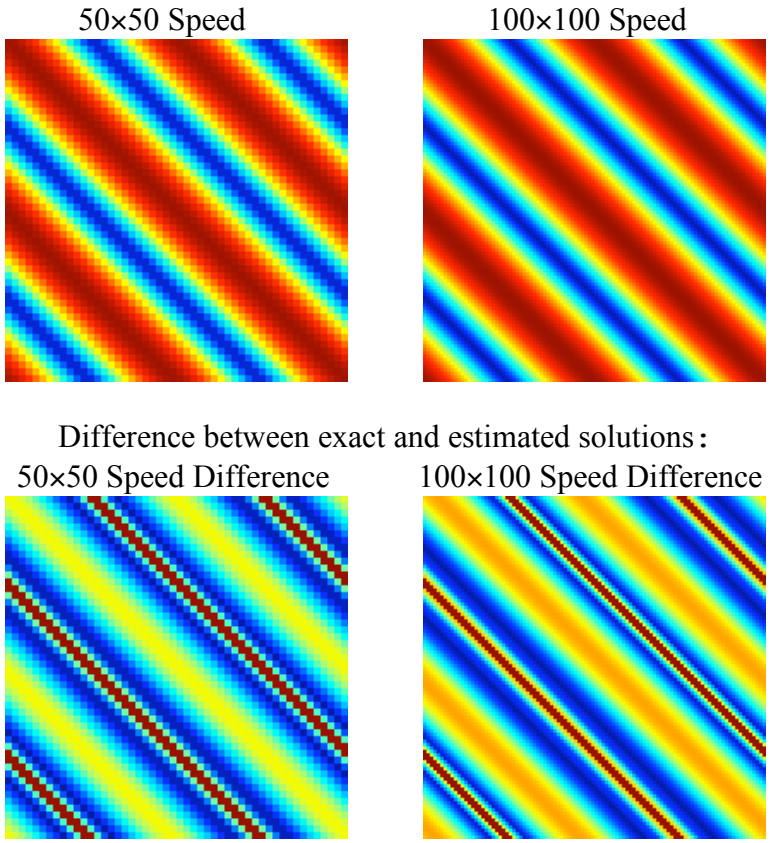

Figure 1d. Plots of the estimated speed (top) and difference between estimated and exact speed (bottom) for the 2-D linear acoustic wave problem at time t = 0.2 s on the two computational meshes considered. The left column has the results on the 50×50 mesh, the right column has results on the 100×100 mesh, both on the unit square. The speed data (top row) range is (dark blue) $0.0 \le u \le 0.000031$ (dark red). The speed difference data (bottom row) range is (dark blue) $0.0 \le u \le \{50\text{: } 1\times10^{-7}\text{; } 100\text{: } 2\times10^{-8}\}$ (dark red). All values are in cm/s. *The estimated solution is extremely close to the exact solution for this problem*.

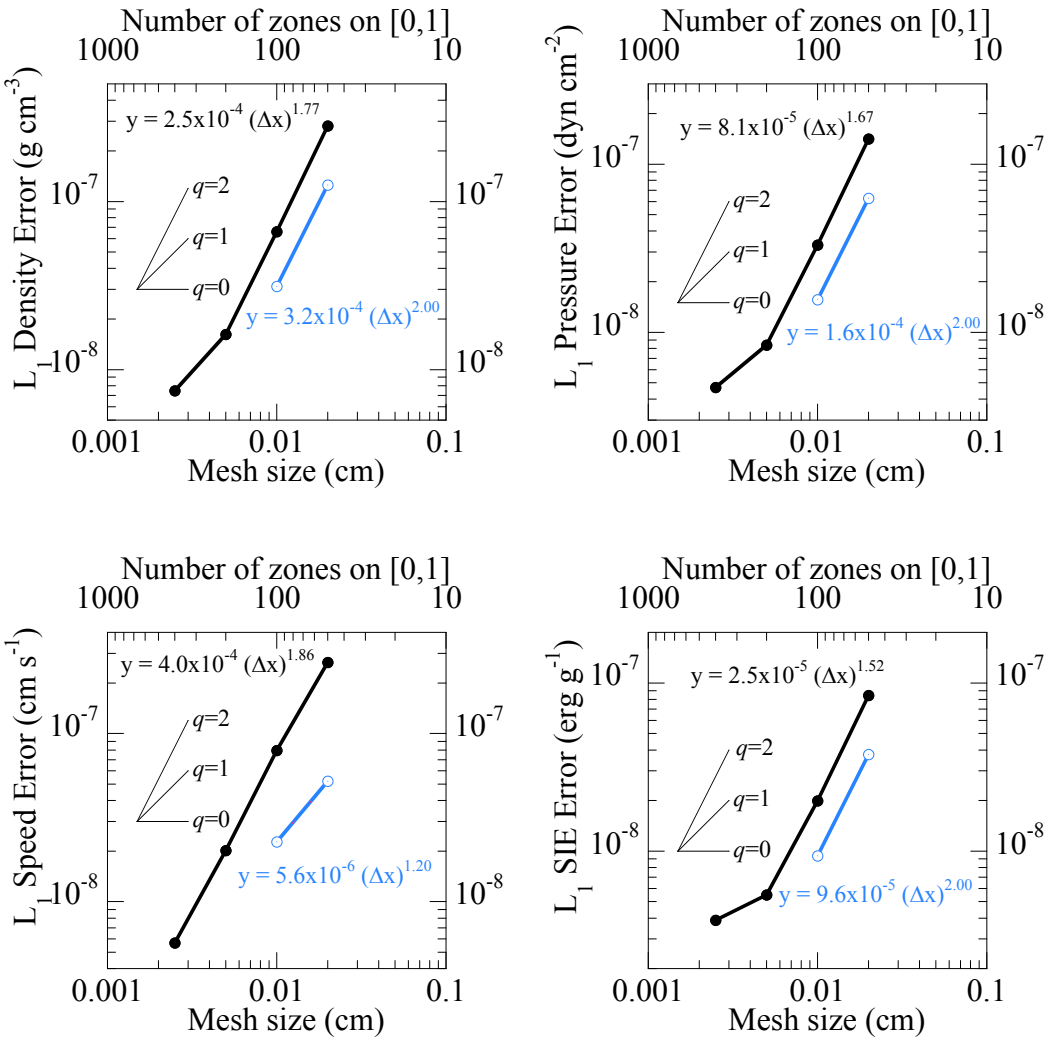

Figure 2. Plots of the L_1 norm of the difference between the exact solution and the computed (i.e., RAGE) solution (in **black** from Table 5), and the L_1 norm of the difference between the exact solution and the estimated solution (in blue from Table 8) are shown. Data is displayed for the 2-D linear acoustic wave problem at $t = 0.2$ s on the four computational meshes considered, for code version 2004-1126*. Clockwise from the upper left, the plots correspond to density, pressure, specific internal energy, and speed. The lines on the left of each plot represent convergence rates of $q = 0$, 1, and 2. The equations give the effective convergence relation associated with each set of data points. The error in the estimated solution is approximately a factor of two smaller than the error in the corresponding RAGE solution.

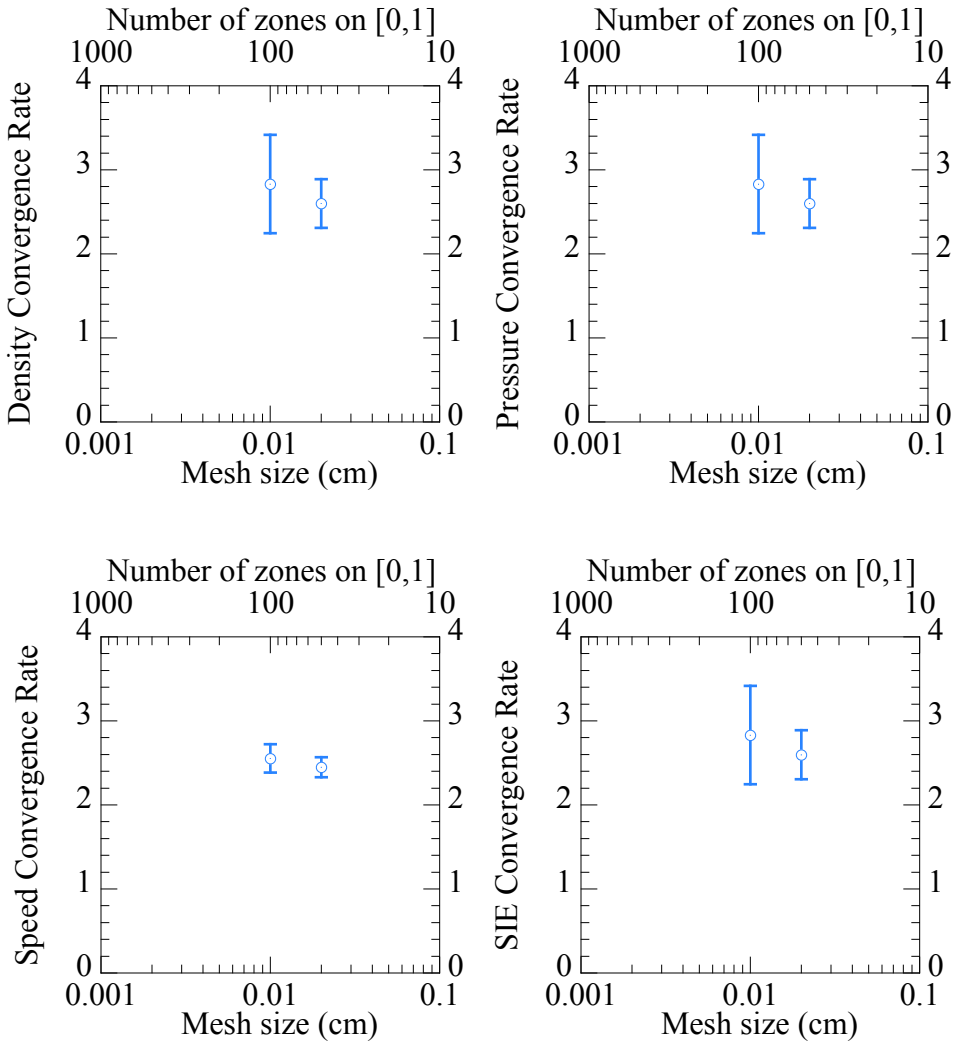

Figure 3. Plots of the mean pointwise convergence rate q from Table 9 for the 2-D linear acoustic wave problem at time $t = 0.2$ s on the two computational meshes for which the estimated solution was obtained. Clockwise from the upper left, results are plotted for the density, pressure, SIE, and speed. The uncertainty bounds in these plots indicate ± one standard deviation in these values, which are calculated from the distribution of convergence rate values on the mesh.

4b. A 2-D nonlinear acoustic wave problem

The nonlinear acoustic wave problem considered is a special case of the problem described in the previous section. Specifically, the domain, boundary conditions, and form of the initial conditions are the same; the only difference is the amplitude of the initial perturbation, which affects only the initial velocity, as indicated in Table 3. With a larger initial perturbation, the nonlinearities evolve and affect the solution at the final time. The waves do not remain sinusoidal, rather they began to steepen.

The problem we consider is specified by the parameters in Table 11, where all other quantities are as in the preceding section. As will be shown, the difference in the amplitude of the perturbation by two orders of magnitude over the problem in the preceding section affects the details of the solution. With these parameters, the calculation was run from an initial time of $t = 0$ s to a final time of $t = 0.2$ s.

Table 11. 2-D nonlinear acoustic wave initial parameters.

γ	k_x	k_y	ω	ε
5/3	2π	2π	2π	10^{-2}

The exact solution of Table 2 is not valid in this case, so one cannot evaluate exact convergence parameters for this problem. We compared the results of the *nonlinear* simulations to the exact *linear* solution to ensure that the problem was indeed nonlinear. The difference was several orders of magnitude larger than for the 2-D linear acoustic wave problem, demonstrating that we were indeed no longer in the linear regime.

Convergence results for the 2-D nonlinear acoustic wave problem are catalogued in Tables 12, 13, and 14. Table 12 contains the global convergence results where the estimated, instead of the exact, solution is used to evaluate the error in the coarse grid, computed solution. As one would expect, global computational error is seen to decrease with zone size. The estimated solution is useful in that it can stand in place of the exact solution when no exact solution is known. Although not as accurate as the exact solution, the estimated solution is still more accurate than the coarse mesh, computed solution. One could question whether or not it would be better to interpolate the fine grid computational solution onto the coarse grid and use it to stand in place of the exact solution.

Tables 13 and 14 contain the mean and standard deviation of, respectively, the computed convergence rate q over the computational mesh, and the corresponding inferred convergence prefactor A. As with the linear problem, the mean quantities increase with decreasing spatial discretization. Note the exceptionally large mean prefactors in the fine zoning case for density, pressure and internal energy, but not for speed in Table 13. We do not know why such anamolously large values are present in this problem. Very large prefactors are present in subsequent problems, however their existence is due to regions of quiescent material. There is no quiescent material in the acoustic wave problems.

We have considered two hypotheses as to why the prefactors may be large. First, note that in Eqs. 2-7, with small zoning, large prefactors result from large convergence rates. Large convergence rates occur when

$$\frac{\xi_m - \xi_c}{\xi_f - \xi_m} >> 1. \tag{4-10}$$

Eqs. 2-7 was derived for an ansatz slightly different than the one we are using. Nevertheless, one could suspect that if the change in the physical quantities going from coarse to medium zoning is much larger than the change going from medium to fine zoning, then the convergence rate in Eqs. 3-1 is very large. Mean convergence rates for the nonlinear acoustic wave problem are close to three, but with a standard deviation of about one. There may therefore be some cells with convergence rates between four and five. For $q = 4{,}5$ the ratio in Eq. 4-10 is on the order of 16-32.

Although the nonlinear acoustic wave problem did not have an exact solution, the linear acoustic wave problem did. Both Table 6 and Figure 2 indicate that the global convergence rate decreased dramatically when the mesh was increased from 200 to 400 cells for density, pressure, and SIE, but not for speed. A sudden decrease in the *intermediate* convergence rate between the medium and fine meshes would result in a large ratio for Eq. 4-10 and a large total convergence rate for the coarse-medium-fine mesh analysis (Table 13). The large convergence rate would then create large prefactors. However, the linear acoustic wave problem did not show large, mean prefactors. Perhaps there was a similar, but more dramatic change in the convergence rate for the nonlinear acoustic wave problem, although it is unclear why convergence rates would change so abruptly with zoning.

An alternative hypothesis is that there are spurious roots for the error ansatz and the Newton solver sometimes converges to these roots instead of the real roots. We hoped by starting the Newton solver close to the calculated solutions to only find the root of interest, but such is not guaranteed.

Global Convergence Results

Table 12. 2-D nonlinear acoustic wave computed-estimated solution error, $t = 0.2$ s.

N_x	Δx (cm)	$\|\hat{\rho} - \rho_{\Delta x}\|_1$ (g cm^{-3})	$\|\hat{p} - p_{\Delta x}\|_1$ (dyne cm^{-2})	$\|\hat{e} - e_{\Delta x}\|_1$ (erg g^{-1})	$\|\hat{u} - u_{\Delta x}\|_1$ (cm s^{-1})
50 (100,200)	0.02	$1.59\tilde{\times}1^{-5}$	$7.96\tilde{\times}1^{-6}$	$4.77\tilde{\times}1^{-6}$	$2.18\tilde{\times}1^{-5}$
100 (200,400)	0.01	$3.84\tilde{\times}1^{-6}$	$1.92\tilde{\times}1^{-6}$	$1.15\tilde{\times}1^{-6}$	$5.88\tilde{\times}1^{-6}$

*RAGE version 2004-1126**

Mean, Pointwise Convergence Results

Table 13. 2-D nonlinear acoustic wave estimated convergence rate q, $t = 0.2$ s.

Range of cells	*Density*	*Pressure*	*Energy*	*Speed*
50 (100,200)	2.59±0.287	2.59±0.288	2.58±0.290	2.44±0.166
100 (200,400)	2.92±1.09	2.92±1.05	2.91±0.987	2.56±0.229

*RAGE version 2004-1126**

Table 14. 2-D nonlinear acoustic wave estimated convergence coefficient A, $t = 0.2$ s.

Range of cells	*Density*	*Pressure*	*Energy*	*Speed*
50 (100,200)	0.938±1.94	0.470±0.977	0.281±0.579	0.334±0.224
100 (200,400)	$(3.89\pm27.3)\times\tilde{1}^{11}$	$(3.46\pm24.3)\times\tilde{1}^{10}$	$(2.00\pm14.0)\times\tilde{1}^{9}$	0.736±0.391

*RAGE version 2004-1126**

Figures 4-6 contain plots that further clarify these results. Figures 4a–d contain plots of the RAGE solution for the density, pressure, speed, and SIE at the final time on the four computational meshes. As for the problem of the previous section, the smooth, oscillatory nature of this solution is once again evident in these images. Figure 5 contains a plot of the L_1 norm of the difference between the estimated solution and the computed solution for the four computational meshes inferred (Table 12). Figure 6 contains plots of the pointwise values of the convergence rate on the two meshes for which the estimated solution was obtained (Tables 13).

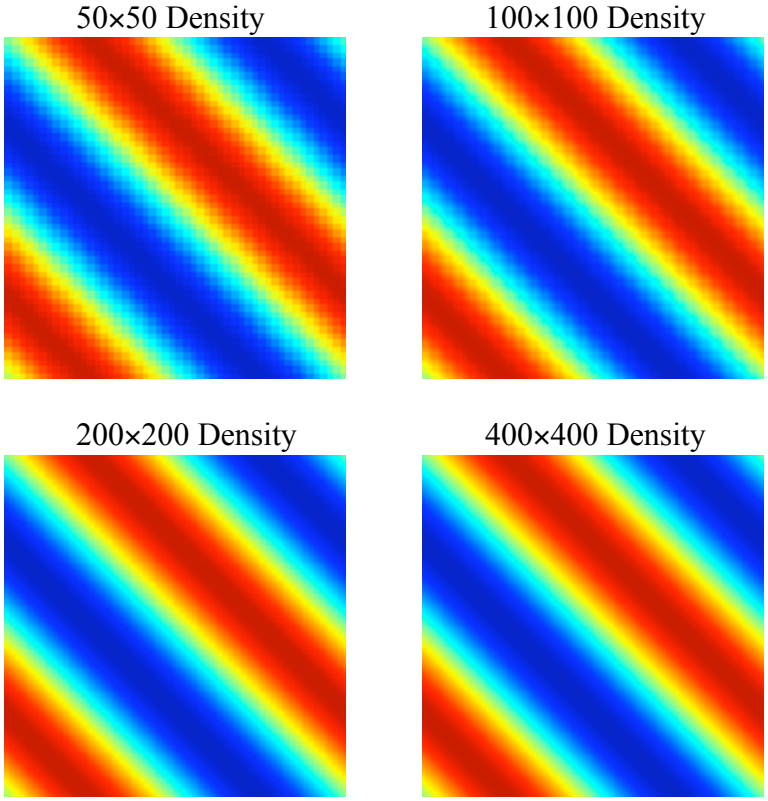

Figure 4a. Plots of the computed density for the 2-D nonlinear acoustic wave problem at time t = 0.2 s on the four computational meshes considered. Clockwise from the upper left, the plots correspond to the 50×50, 100×100, 400×400, and 200×200 meshes on the unit square. The data range is (dark blue) $0.985 \leq \rho \leq 1.015$ (dark red); all values are in g/cm^3. Recall that $\rho \equiv 1.0$ uniformly at $t = 0$ and evolves into a sinusoidal wave with small perturbations around the initial condition. The refinement in the solution is evident with increasing zoning.

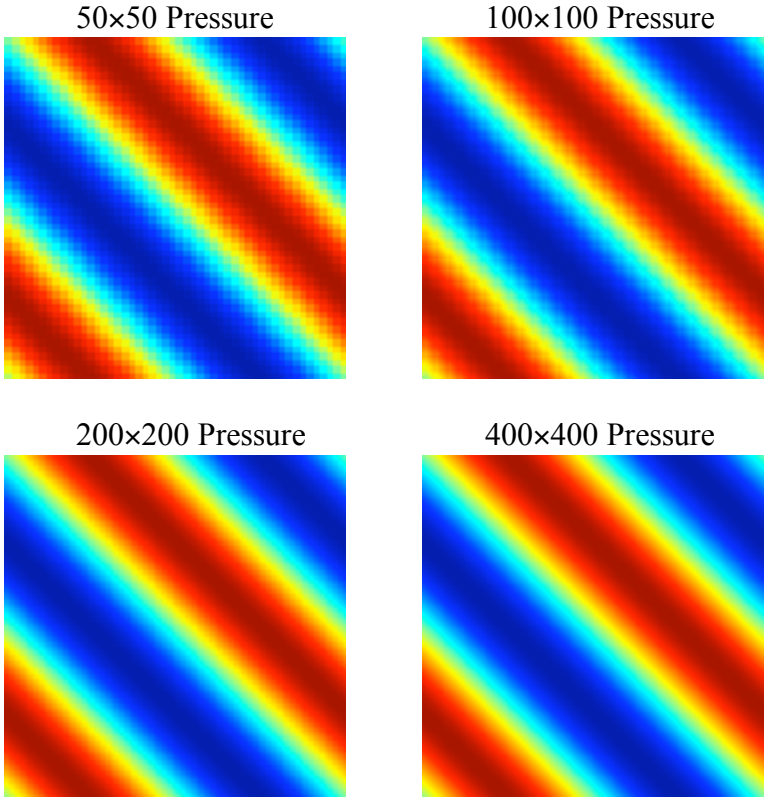

Figure 4b. Plots of the computed pressure for the 2-D nonlinear acoustic wave problem at time $t = 0.2$ s on the four computational meshes considered. Clockwise from the upper left, the plots correspond to the 50×50, 100×100, 400×400, and 200×200 meshes on the unit square. The data range is (dark blue) $0.293 \leq p \leq 0.307$ (dark red); all values are in dyne/cm^2. Recall that $p \equiv 0.3$ uniformly at $t = 0$ and evolves into a sinusoidal wave with small perturbations around the initial condition. The refinement in the solution is evident with increasing zoning.

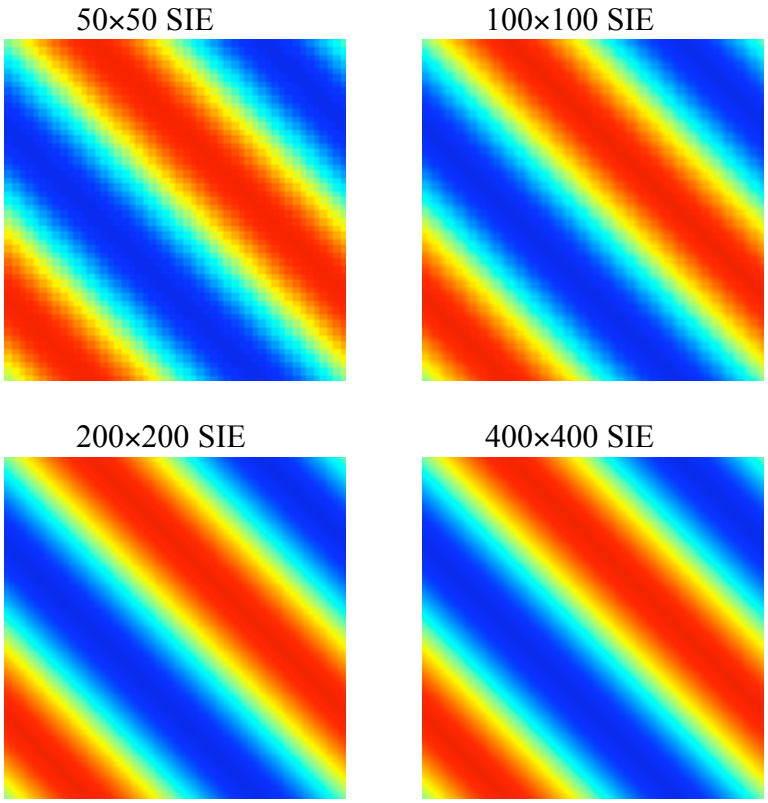

Figure 4c. Plots of the computed SIE for the 2-D nonlinear acoustic wave problem at time t = 0.2 s on the four computational meshes considered. Clockwise from the upper left, the plots correspond to the 50×50, 100×100, 400×400, and 200×200 meshes on the unit square. The data range is (dark blue) $0.445 \le e \le 0.455$ (dark red); all values are in erg/g. Recall that $e \equiv 9/20$ uniformly at t = 0 and evolves into a sinusoidal wave with small perturbations around the initial condition. The refinement in the solution is evident with increasing zoning.

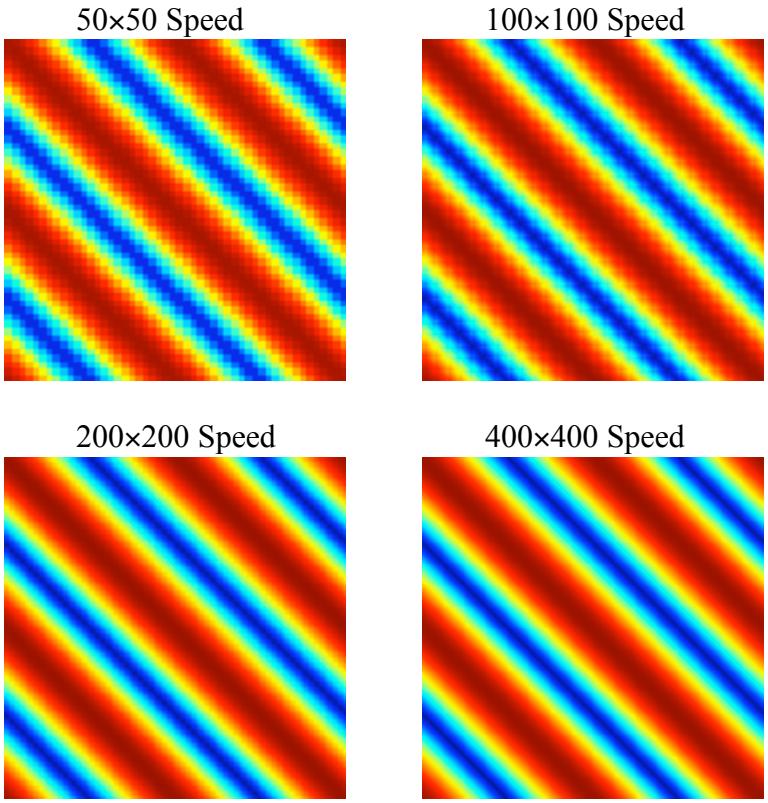

Figure 4d. Plots of the computed speed for the 2-D nonlinear acoustic wave problem at time t = 0.2 s on the four computational meshes considered. Clockwise from the upper left, the plots correspond to the 50×50, 100×100, 400×400, and 200×200 meshes on the unit square. The data range is (dark blue) $0.0 \le u \le 0.0031$ (dark red); all values are in cm/s. Recall that $0.0 \le u \le 0.01$ at t = 0. The refinement in the solution is evident with increasing zoning.

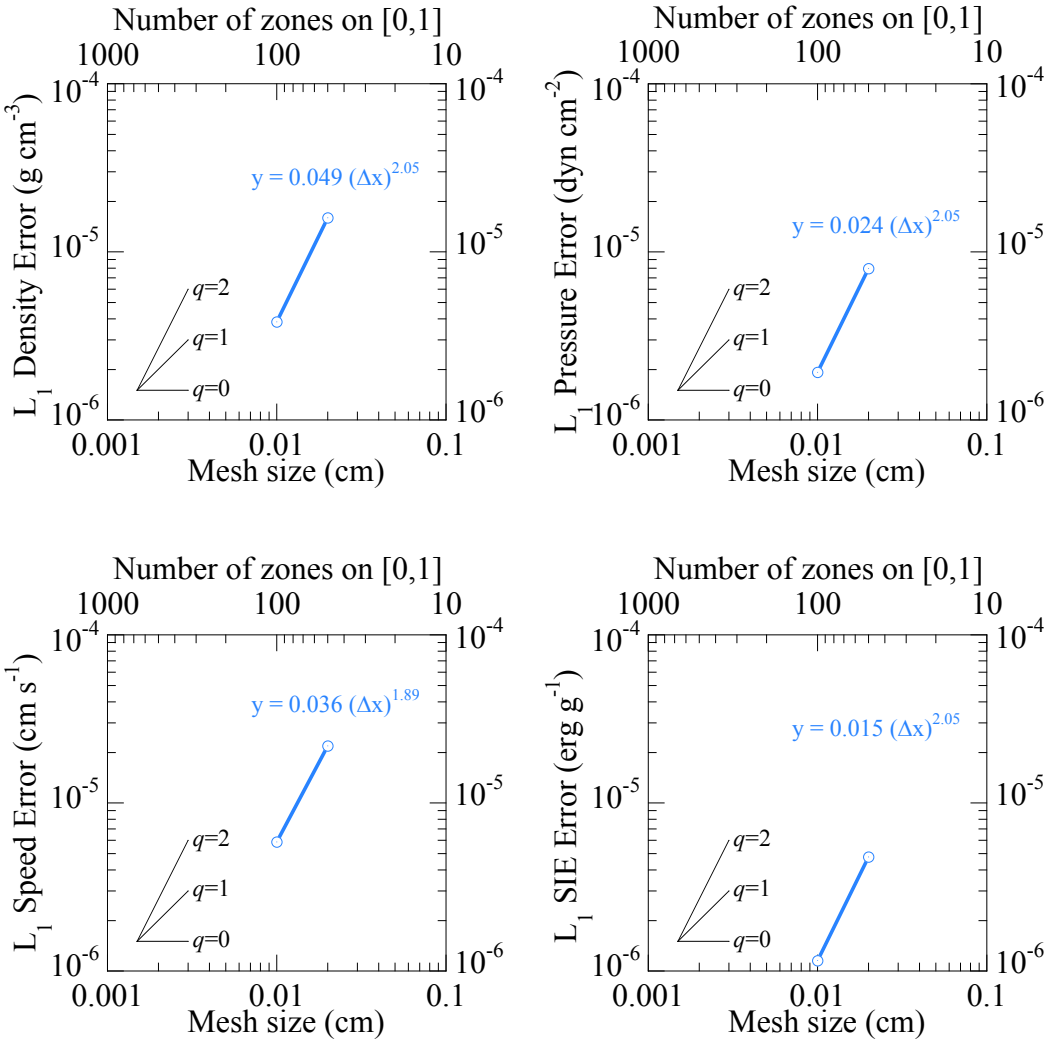

Figure 5. Plots of the effective error for the 2-D nonlinear acoustic wave problem at time $t = 0.2$ s on the two computational meshes for which the estimated solution was obtained (Table 12). *Although it appears visually similar, this is a different kind of data than that shown in Figures 2 and 9*. Clockwise from the upper left, results are plotted for the density, pressure, SIE, and speed. The lines in the lower left of each plot represent convergence rates of q=0, 1, and 2. The equation in blue gives the effective convergence relation associated with the two data points in each plot.

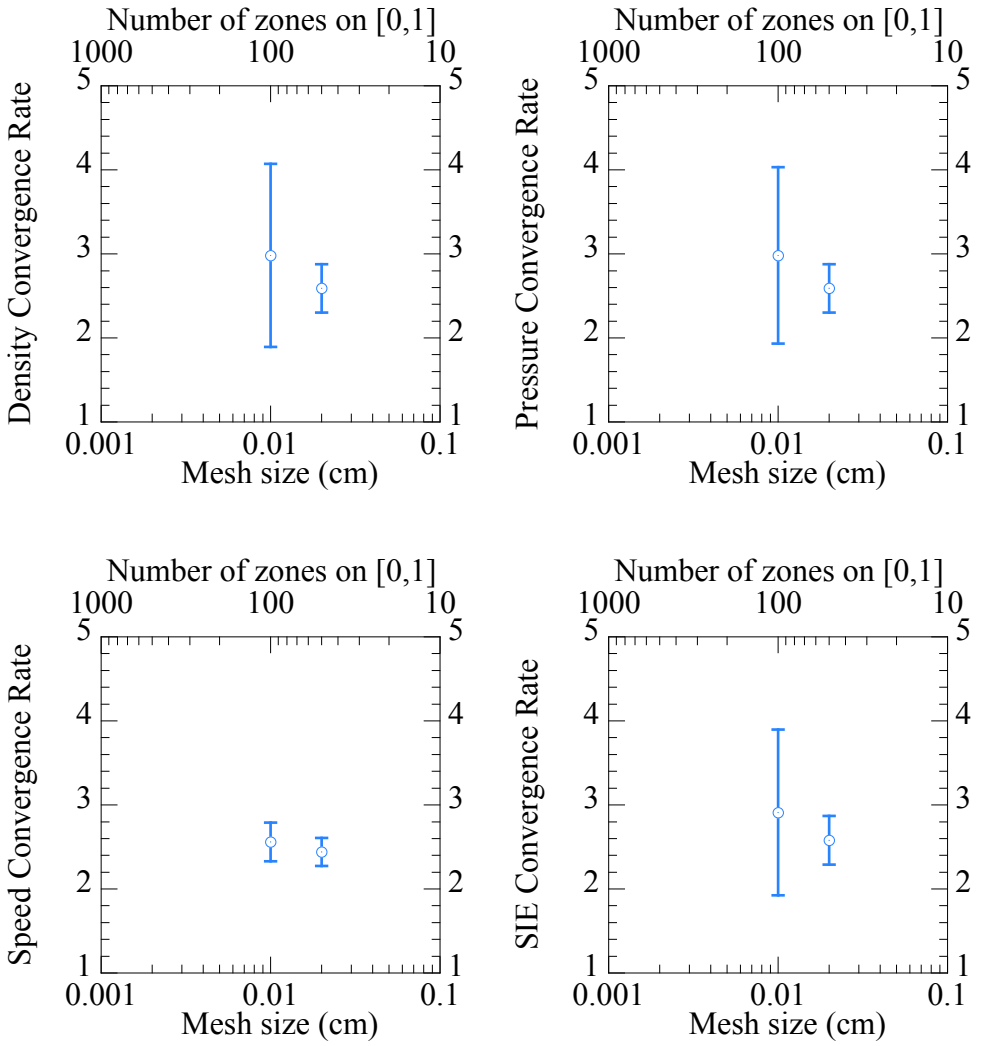

Figure 6. Plots of the mean convergence rate q for the 2-D nonlinear acoustic wave problem at time t = 0.2 s on the two computational meshes for which the estimated solution was obtained (Table 13). Clockwise from the upper left, results are plotted for the density, pressure, SIE, and speed. The uncertainty bounds in these plots indicate ± one standard deviation in these values, which are calculated from the distribution of convergence rate values on the mesh.

4c. A 1-D Riemann problem

The 1-D Riemann (i.e., shock tube) problem for a polytropic gas is a workhorse in the field of hydrodynamics algorithms for both methods development and verification. This problem plays such an important role because it manifests key nonlinearities and discontinuities while possessing a solution that can be directly evaluated for polytropic gases. Moreover, it is very easy to initialize simulation codes for this problem, which consists initially of two constant, uniform states separated at an internal boundary. The computational boundaries are sufficiently far removed from the developing wave interactions as to be irrelevant to the region of interest. Although the solution to this problem cannot generally be obtained in closed form, it is directly computable, requiring the iterative numerical solution of a nonlinear equation; see [Got88] for a detailed explanation of this problem.

There are several possibilities for the structure of the solution to the 1-D Riemann problem. These solutions involve combinations of shock waves, rarefaction fans, and contact discontinuities. We consider the case in which a rarefaction fan, a contact discontinuity, and a shock wave develop. The initial conditions for the case we consider are given in Table 15.

Table 15. 1-D Riemann problem initial conditions, with $\gamma = 1.4$.

	ρ (g cm^{-3})	p (dyne cm^{-2})	e (erg g^{-1})	u (cm s^{-1})
$x < 0.5$	1.00	1.00	2.50	0.00
$x > 0.5$	2.25	1.80	2.00	0.00

This problem was run on the domain $0 < x < 1$, with meshes of 20, 40, 80, and 160 zones. The exact solution was computed using an algorithm based on the paper of Gottlieb & Groth [Got88].[3] The solution was compared at a single time of $t = 0.2$ s. Plots of the exact and computed solutions at this time are given in Fig. 7. The plots in this figure suggest qualitatively that the calculations are converging, since the computed solutions appear to approach the exact solutions as the mesh becomes finer.

[3] See also the work of Quartapelle et al. [Qua03] for an approach to the exact solution of the 1-D Riemann problem for more general equations of state.

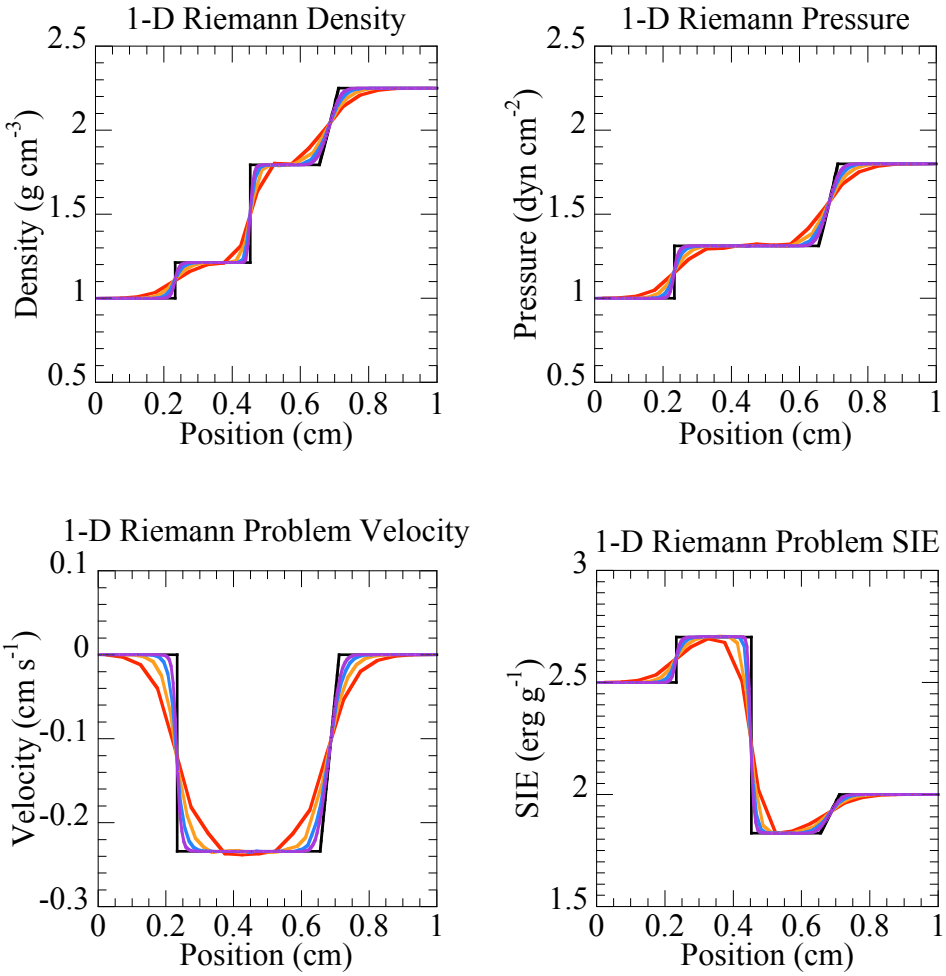

Figure 7. Plots of the exact and computed solution for the 1-D Riemann problem, for the initial conditions given in Table 15, at the final time $t = 0.2$ s. The exact solution is the **black** line and the computed solution is given for 20 (red), 40 (gold), 80 (blue), and 160 (purple) points on the unit interval. Clockwise from the upper left, the following quantities are plotted: density, pressure, SIE, and x-velocity. Qualitatively, these plots suggest convergence, since the computed solution approaches the exact solution as the mesh becomes finer.

Table 16 catalogues the global L_1 global error between the exact and computed (RAGE) solution for key physical variables. These values are computed based on the grids delineated by the number and dimension of the computational cells indicated in the first two columns of this table. An important aspect of the table is in showing how the error changes with zoning, not in the magnitude of the error itself. The norm values can be used to compute the pair-wise convergence rate q and convergence prefactor A for these results. Those values, compiled in Tables 17 and 18, all indicate convergent calculations. In particular, the convergence rates, which vary between ~0.6 and ~0.9, are consistent both with a theoretical maximum convergence rate of unity for this problem [Kim95, Eng98] as well as with previous experience on convergence analysis for problems containing shocks. Note that x-velocity is used in this problem in place of speed. For density and pressure, the convergence rate and prefactor increase with decreasing zone size, the opposite of the linear acoustic wave problem; this and may have to do with the increase in resolution of the rarefaction wave. The convergence rate and prefactor for energy and x-velocity show no discernable trend. The velocity and SIE both contribute to the total energy. Assuming that the error for total energy was decreasing steadily, the error for the velocity and SIE could be shifting somewhat between the SIE and velocity as the zoning is refined.

Global Convergence Results

Table 16. 1-D Riemann problem exact-computed L_1 errors at $t = 0.2$ s.

N_x [0,1]	Δx (cm)	$\left\|\rho^* - \rho_{\Delta x}\right\|_1$ (g cm^{-3})	$\left\|p^* - p_{\Delta x}\right\|_1$ (dyne cm^{-2})	$\left\|e^* - e_{\Delta x}\right\|_1$ (erg g^{-1})	$\left\|u_x^* - u_{x\Delta x}\right\|_1$ (cm s^{-1})
20	0.05	4.10×10^{-2}	3.59×10^{-2}	3.73×10^{-2}	2.18×10^{-2}
40	0.025	2.59×10^{-2}	2.11×10^{-2}	2.32×10^{-2}	1.24×10^{-2}
80	0.0125	1.59×10^{-2}	1.20×10^{-2}	1.43×10^{-2}	7.29×10^{-3}
160	0.00625	9.25×10^{-3}	6.28×10^{-3}	9.63×10^{-3}	3.72×10^{-3}

RAGE version 2004-1126

Table 17. 1-D Riemann problem exact-computed convergence rate q at $t = 0.2$ s.

Range of cells	*Density*	*Pressure*	*SIE*	*x-Velocity*
20,40	6.60×10^{-1}	7.67×10^{-1}	6.80×10^{-1}	8.17×10^{-1}
40,80	7.09×10^{-1}	8.08×10^{-1}	7.05×10^{-1}	7.66×10^{-1}
80,160	7.78×10^{-1}	9.40×10^{-1}	5.67×10^{-1}	9.68×10^{-1}

RAGE version 2004-1126

Table 18. 1-D Riemann problem exact-computed convergence prefactor A at $t = 0.2$ s.

Range of cells	*Density*	*Pressure*	*SIE*	*x-Velocity*
20,40	2.96×10^{-1}	3.58×10^{-1}	2.86×10^{-1}	2.52×10^{-1}
40,80	3.54×10^{-1}	4.16×10^{-1}	3.13×10^{-1}	2.09×10^{-1}
80,160	4.80×10^{-1}	7.40×10^{-1}	1.71×10^{-1}	5.07×10^{-1}

RAGE version 2004-1126

The first two rows in Table 16 are to be compared to the values in Table 19, which follows. That table contains the L_1 norms of the difference between the exact solution and the estimated solution that is calculated as a solution to the method outlined in §3 for the indicated meshes (recall that computed values on three different meshes are required to infer an estimated solution on the coarsest mesh). Comparing the errors presented in these two tables, three important aspects of the global norm of the estimated solution are to be seen. First, it is approximately a factor of two smaller than the global norm of the computed solution on the same mesh. Second, it is slightly smaller than the global norm of the computed solution on the next finer mesh. Third, it is seen to be greater than the global norm of the computed solution on the finest mesh with which the estimated solution was calculated.

Table 19. 1-D Riemann problem exact-estimated solution error at $t = 0.2$ s.

N_x	Δx (cm)	$\left\|\rho^* - \hat{\rho}\right\|_1$ (g cm^{-3})	$\left\|p^* - \hat{p}\right\|_1$ (dyne cm^{-2})	$\left\|e^* - \hat{e}\right\|_1$ (erg g^{-1})	$\left\|u_x^* - \hat{u}_x\right\|_1$ (cm s^{-1})
20 (40,80)	0.05	1.97×10^{-2}	1.62×10^{-2}	1.78×10^{-2}	9.95×10^{-3}
40 (80,160)	0.025	1.28×10^{-2}	9.52×10^{-3}	1.14×10^{-2}	5.90×10^{-3}

RAGE version 2004-1126

Table 20 contains the mean and standard deviation of the computed convergence rate q for the indicated computational mesh, while Table 21 contains the corresponding values for the inferred convergence prefactor A. That the standard deviations are comparable to—if not greater than—the means suggests that these simple measures are poor statistics with which to characterize these distributions. Recall that these values are calculated using only those mesh points for which a convergence rate is obtained.

The values of the prefactor for fine zoning in Table 21 are extremely large, as was previously seen in the nonlinear acoustic wave problem in Table 14, however for a different reason. Both the 1- and 2-D Riemann problems had quiescent regions where very little change occurred during the simulation. Figures 11 and 12 show how the convergence rate and prefactor both increased dramatically in these regions of little interest, resulting in very large average convergence rates, prefactors and standard deviations for all physical quantities. One possible solution to this problem of data pollution from quiescent regions would have been to include a mask when averaging the convergence rates and prefators, such that only cells that contribute significantly to the error are counted in the average. The quiescent regions have cells that contribute negligibly to the computational error.

Mean, Pointwise Convergence Results

Table 20. 1-D Riemann problem estimated convergence rate q at $t = 0.2$ s.

Range of cells	*Density*	*Pressure*	*Energy*	*x-Velocity*
20 (40,80)	2.92±2.02	3.10±2.00	2.93±2.05	3.06±1.91
40 (80,160)	4.11±3.77	4.40±3.33	4.26±3.51	4.06±3.03

RAGE version 2004-1126

Table 21. 1-D Riemann problem estimated convergence coefficient A at $t = 0.2$ s.

Range of cells	*Density* ($\times 10^5$)	*Pressure* ($\times 10^5$)	*Energy* ($\times 10^5$)	*x-Velocity*
20 (40,80)	$(5.59\pm23.9)\times10^{5}$	$(6.32\pm26.7)\times10^{5}$	$(2.13\pm8.51)\times10^{5}$	$(1.88\pm7.12)\times10^{4}$
40 (80,160)	$(6.49\pm38.9)\times10^{19}$	$(1.89\pm11.3)\times10^{15}$	$(6.29\pm36.5)\times10^{14}$	$(2.71\pm15.9)\times10^{13}$

RAGE version 2004-1126

Figures 8–12 shed further light on these results. Figures 8a and 8b contain plots, respectively, for the 20/40/80 and 40/80/160 cases, of the pointwise absolute difference between the exact solution and the estimated solution for the physical variables on the meshes for which the estimated solution was obtained. In these plots, the exact solution is indicated as a **black** line, the estimated solution as a blue line, the calculated (RAGE) solution as a red line, and the pointwise error (plotted against the right ordinate) as a purple line. The dashed red lines around the calculated solution in these plots correspond to the values $\pm A\Delta x^p$ about those values. The dashed lines can give one a sense of the magnitude of error in the computed solution. Notice that the dashed lines from the error ansatz *do not* always encompass the exact solution, however, they do indicate where the error is greatest.

Not unexpectedly, the greatest difference between the estimated solution and the exact solution occurs where the solution has discontinuities in slope, i.e., at the shock, the head and tail of the rarefaction, and, in the case of density and SIE, the contact. The difference between the 20/40/80 (8a) and 40/80/160 (8b) cases are that the discontinuities are better localized in the higher resolution case, which also has errors that are generally slightly greater in absolute magnitude than those of the lower resolution case.

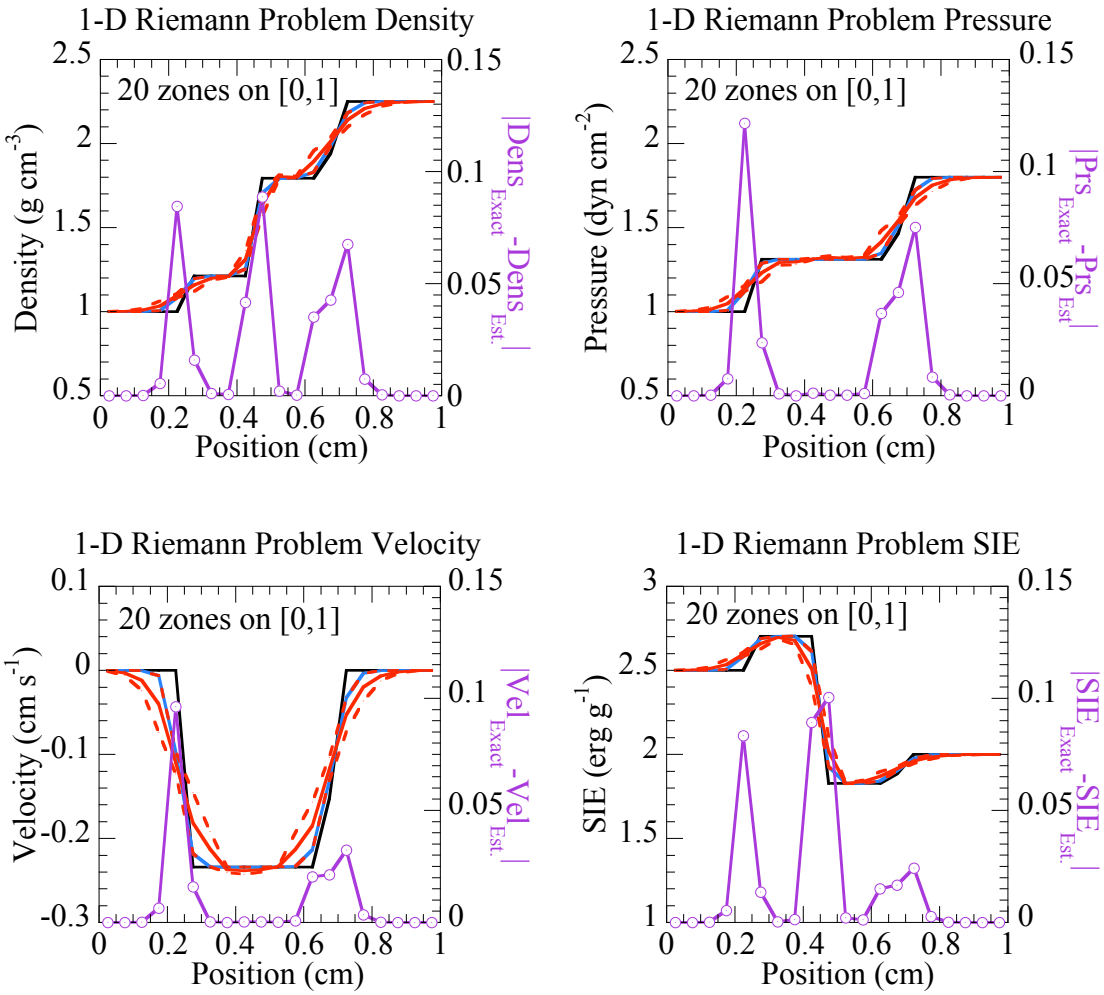

Figure 8a. Solutions and absolute difference between the exact and estimated solutions for the 1-D Riemann problem on the 20-zone base computational mesh at t = 0.2 s. Clockwise from the upper left, the following quantities are plotted: density, pressure, SIE, and x-velocity. The exact solution on this mesh (in **black**), the estimated solution (in blue), and the calculated solution (in red) are plotted against the left ordinate, while the difference between these solutions (in purple) is plotted against the right ordinate. The dashed lines (in red) indicate values that are $\pm A\Delta x^p$ relative to the calculated solution. Notice that the error is highest at the discontinuities.

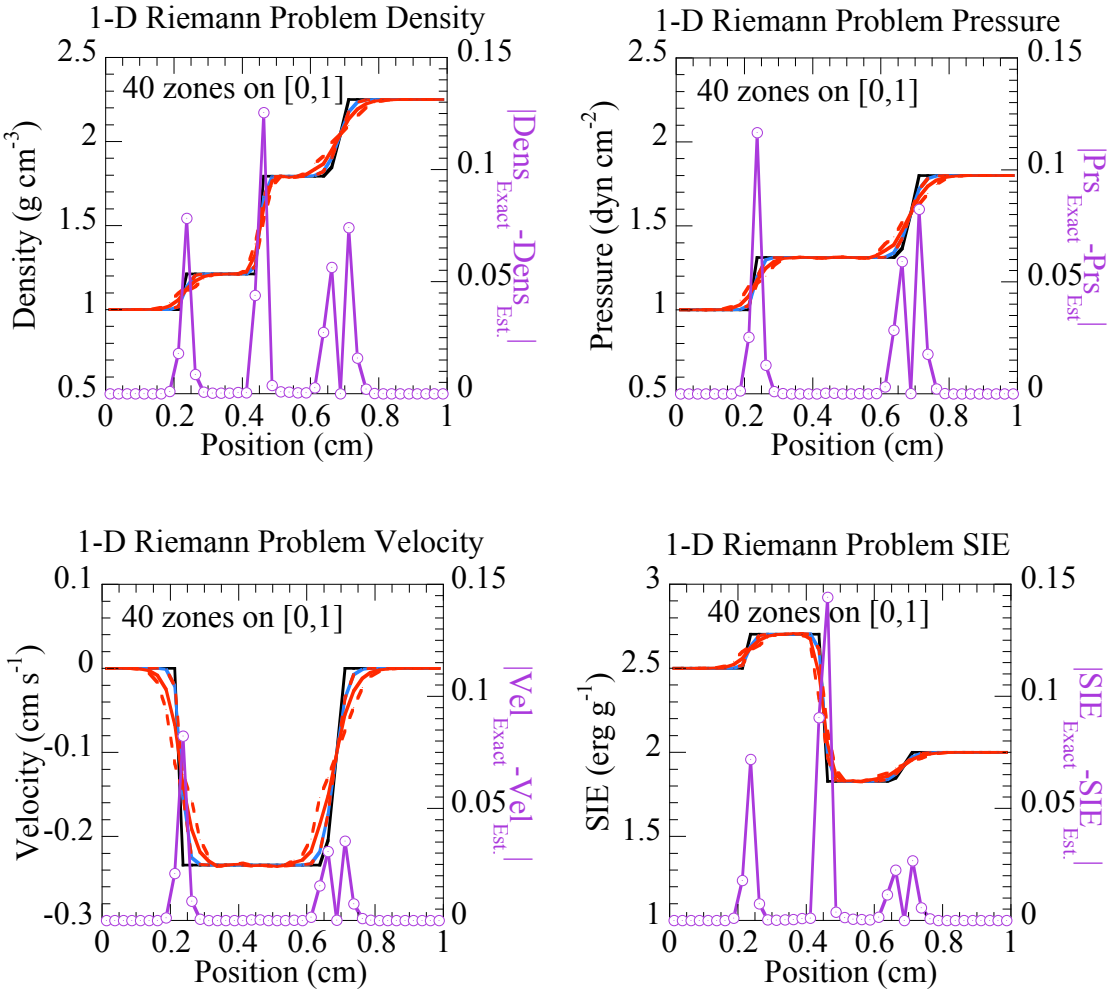

Figure 8b. Plots of the absolute difference between the exact and estimated solutions for the 1-D Riemann problem on the 40-zone base computational mesh at t = 0.2 s. Clockwise from the upper left, the following quantities are plotted: density, pressure, SIE, and x-velocity. The exact solution on this mesh (in **black**), the estimated solution (in blue), and the calculated solution (in red) are plotted against the left ordinate, while the difference between these solutions (in purple) is plotted against the right ordinate. The dashed lines (in red) indicate values that are $\pm A\Delta x^p$ relative to the calculated solution. Notice that the error is highest at the discontinuities.

Figure 9 contains plots of the data in Tables 16 and 19. The **black** values in these plots are the L_1 norm of the difference between the exact solution and the computed solution as a function of the mesh size for the four computational meshes. The blue values in these plots are the L_1 norm of the difference between the exact solution and the estimated solution as a function of the mesh size for the four computational meshes. For reference, in the lower left-hand corner of these plots are straight lines corresponding to convergence rates of zero, one, and two. For the estimated solution, no contribution to the L_1 norm is accrued for points that did not converge. These plots graphically depict the important result to be inferred from Tables 16 and 19, viz., that the error in the estimated solution is approximately a factor of two smaller than the error in the RAGE solution at the same mesh resolution. Moreover, the error in the estimated solution is smaller than the error in the RAGE solution at one-half the mesh resolution.

Figure 10 contains plots of the data in Table 20, viz., the mean convergence rates plus or minus one standard deviation, as a function of the base mesh size. The variance shown in these values can be understood from the results plotted in Fig. 11, which shows the pointwise convergence rate as a function of ordinate of cell-centered position in the mesh. Specifically, Figs. 11a and 11b contain plots, respectively, for the 20/40/80 and 40/80/160 cases, of the pointwise convergence rate q (in purple) together with the estimated solution (in blue) and the computed solution on the same mesh (in red).These plots indicate that the local convergence rate (plotted against the right ordinate) is, overall, notably greater than the theoretical convergence rate of unity, except near the discontinuities, where it does drop to that value. Interior to the developing wave structure, the convergence rate is quite high (say, above two). In the region of nominally quiescent flow, i.e. before the shock and beyond the rarefaction, values in the computed solution that deviate slightly from the unperturbed values lead to the extremely high convergence rates. It is the nature of the distribution of these values that contributes to the large standard deviations in Table 20.

In the finer resolution case (40/80/160, Fig. 11b), there were a small number of points at which the procedure did not converge; these points were given artificially low convergence rate values and appear as drop-outs on these plots. Visual comparison of the estimated (blue) and corresponding computed (red) solution clearly demonstrates that our technique produces estimated solutions with "tighter" discontinuities and that are arguably qualitatively superior to the computed solution at the same mesh resolution.

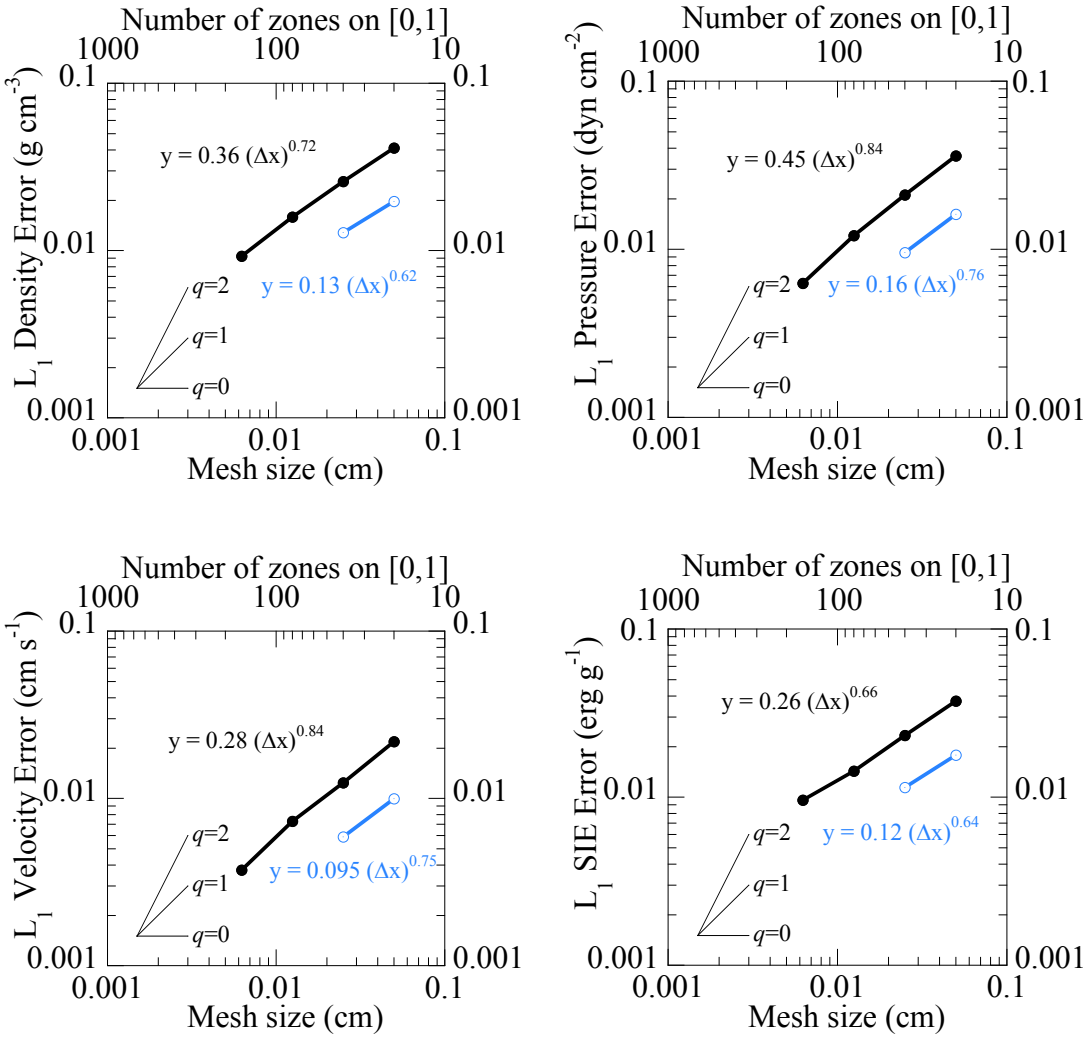

Figure 9. Plots of the L_1 norm of the difference between the exact solution and the computed (i.e., RAGE) solution (in **black**) and the estimated solution and the computed solution (in blue) over the various computational meshes for the 1-D Riemann problem at t=0.2 s on the four computational meshes considered, for code version 2004-1126 (Tables 16 and 19). Clockwise from the upper left, the plots correspond to density, pressure, specific internal energy, and velocity. The lines in the lower left of each plot represent convergence rates of q = 0, 1, and 2. The equations give the effective convergence relation associated with each set of data points. The error in the estimated solution is approximately a factor of two smaller than the error in the corresponding RAGE solution; in fact, the error in the estimated solution is smaller than the error in the RAGE solution at one-half the mesh resolution.

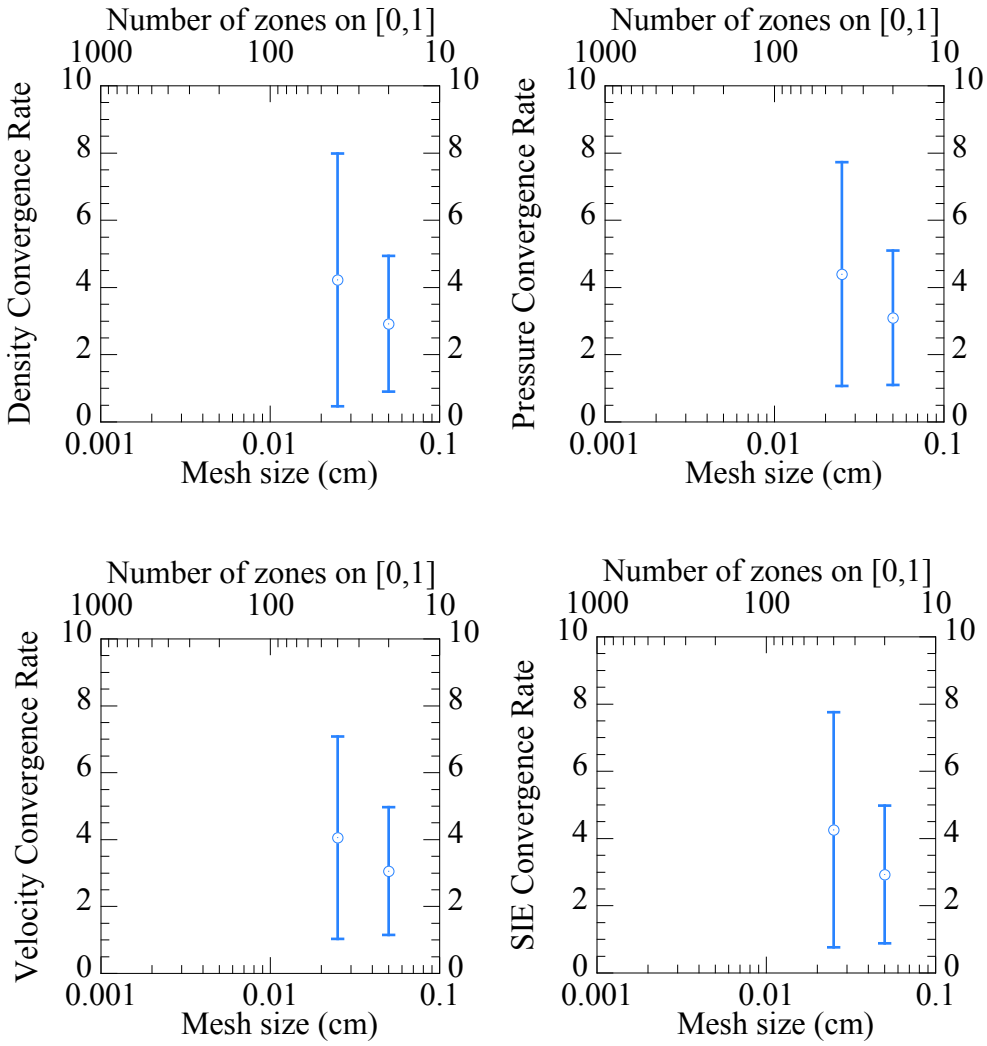

Figure 10. Plots of the mean convergence rate q for the 1-D Riemann problem at time t = 0.2 s on the two computational meshes for which these values were obtained (Table 20). Clockwise from the upper left, results are plotted for the density, pressure, SIE, and x-velocity. The uncertainty bounds in these plots indicate ± one standard deviation in these values, which are calculated from the distribution of convergence rate values on the mesh.

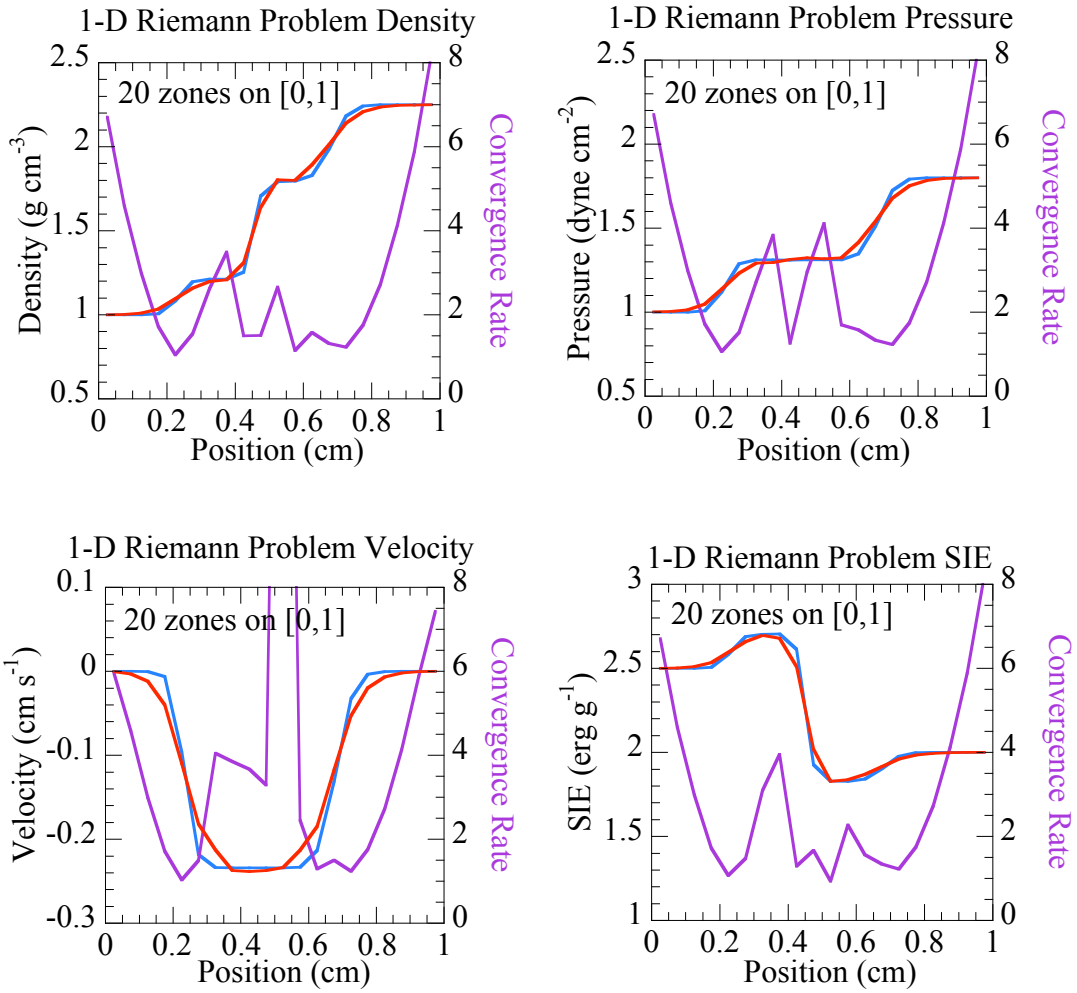

Figure 11a. Plots of the pointwise convergence rate q for the 1-D Riemann problem estimated from the 20-, 40-, and 80-zone computational meshes at $t = 0.2$ s. The estimated solution (in blue) and the computed solution (in red) are plotted against the left ordinate, while the pointwise convergence rate (in purple) is plotted against the right ordinate. Clockwise from the upper left, the following quantities are plotted: density, pressure, SIE, and x-velocity.

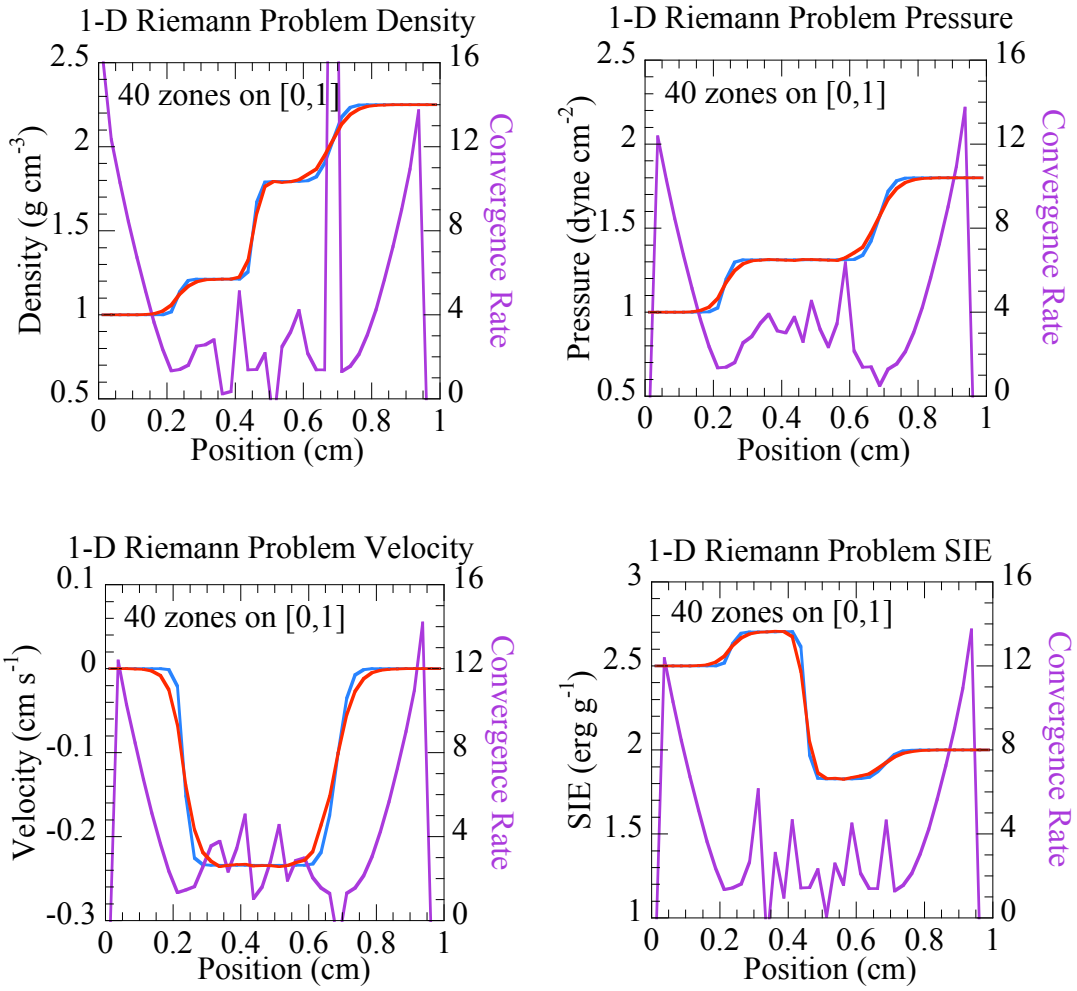

Figure 11b. Plots of the pointwise convergence rate q for the 1-D Riemann problem estimated from the 40-, 80-, and 160-zone computational meshes at $t = 0.2$ s. The estimated solution (in blue) and the computed solution (in red) are plotted against the left ordinate, while the pointwise convergence rate (in purple) is plotted against the right ordinate. Clockwise from the upper left, the following quantities are plotted: density, pressure, SIE, and x-velocity.

Figures 12a and 12b contain plots for the 20/40/80 and 40/80/160 cases, respectively, of the estimated solution (in blue), the computed solution on the same mesh (in red), and the pointwise convergence prefactor A (in purple against a logarithmic axis). As shown in these plots, the local convergence prefactor (plotted against the right ordinate) varies significantly in value. The few-order-of-magnitude variation of the convergence prefactor within the developing wave structure is expected, based on previous experience. The extreme values in the regions of ostensibly quiescent flow, however, are surprising. These values are, in some sense, anomalous, and suggest that the statistics of this quantity are significantly non-Gaussian over these meshes; consequently, the sample mean and variance provide poor characterizations of these data. It is the nature of the distribution of these values that contributes to the large standard deviations in Table 21.

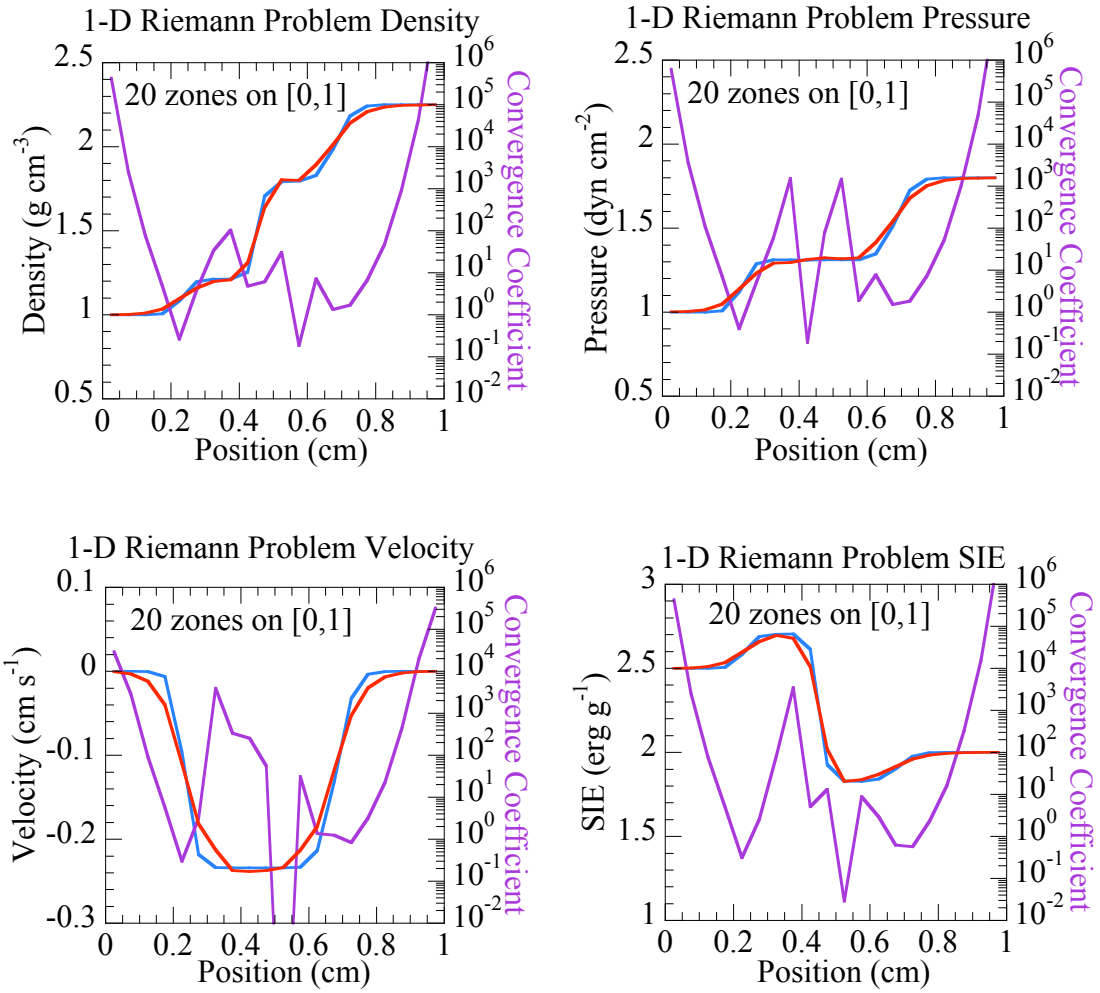

Figure 12a. Plots of the pointwise convergence prefactor A for the 1-D Riemann problem estimated from the 20-, 40-, and 80-zone computational meshes at t = 0.2 s. The estimated solution (in blue) and the computed solution (in red) are plotted against the left ordinate, while the pointwise convergence rate (in purple) is plotted against the right ordinate. Clockwise from the upper left, the following quantities are plotted: density, pressure, SIE, and x-velocity.

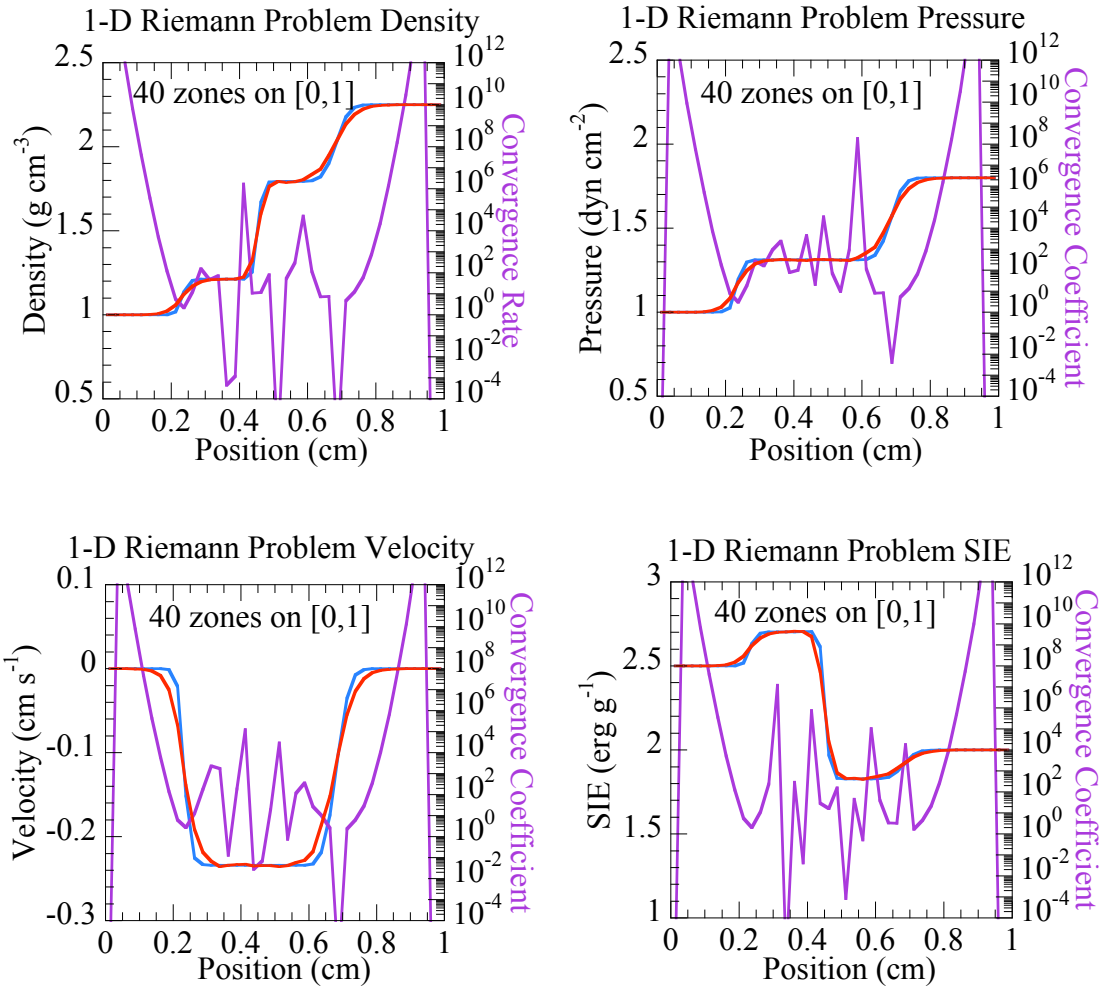

Figure 12b. Plots of the pointwise convergence prefactor A for the 1-D Riemann problem estimated from the 40-, 80-, and 160-zone computational meshes at t=0.2 s. The estimated solution (in blue) and the computed solution (in red) are plotted against the left ordinate, while the pointwise convergence rate (in purple) is plotted against the right ordinate. Clockwise from the upper left, the following quantities are plotted: density, pressure, SIE, and x-velocity.

4d. A 2-D Riemann problem

The 2-D Riemann problem for an inviscid, non-heat-conducting, polytropic gas is a geometrical extension of the 1-D shock tube problem. More precisely, instead of two regions of uniform initial values, the four quadrants of the 2-D plane are initially assigned different, uniform states that evolve under the dynamics of the governing Euler equations. Unlike the 1-D case, however, there is no exact solution for the 2-D Riemann problem; nevertheless, it has engendered much interest in the computational applied mathematics community. The richness of the numerically determined solution structures hints at significant complexity in the solution space for multidimensional gas dynamics problems.

Recent numerical evidence suggests that 19 fundamentally different patterns or types of structures can develop for the 2-D Riemann problem for a polytropic gas [Lax98,Sch93a,Sch93b]. Two of these solutions consist solely of rarefactions, two consist solely of shocks, and two consist solely of contact discontinuities (i.e., slip lines); the remaining solutions develop from combinations of these fundamental waves. We consider one of the all-rarefaction cases in our analysis. The domain of interest is the unit square $\Omega \equiv \{(x,y):(x,y)\in[0,1]\times[0,1]\}$; the full computational domain, however, is $\overline{\Omega} \equiv \{(x,y):(x,y)\in[-1,2]\times[-1,2]\} \supset \Omega$, so that effects of the computational boundary $\partial\overline{\Omega}$ do not influence the calculated solution in Ω at the time of interest. With the four initial regions of the domain of interest numbered I–IV counter-clockwise from the upper right (i.e., I $\equiv \{(x,y): x>0.5 \text{ and } y>0.5\}$, II $\equiv \{(x,y): x\le 0.5 \text{ and } y>0.5\}$, etc.), the initial conditions for this problem are given in Table 22. The meshes we consider had 32x32, 64x64, 128x128, and 256×256 cells in them. We evaluate the solution at the final time of t = 0.2, as considered in [Lax98].

Table 22. 2-D Riemann rarefaction problem initial conditions, with $\gamma = 1.4$.

Region	ρ (g cm^{-3})	p (dyne cm^{-2})	e (erg g^{-1})	u (cm s^{-1})	v (cm s^{-1})
I	1.0	1.0	2.5	0.0	0.0
II	0.5197	0.4	1.9242	-0.7259	0.0
III	0.1072	0.0439	1.0238	-0.7259	1.4045
IV	0.2579	0.15	1.4541	0.0	-1.4045

As for the 2-D nonlinear acoustic wave problem of §4b, there is no exact solution to this problem. We catalogue the convergence results in Tables 23 and 24, which contain, respectively, the mean and standard deviation of the computed convergence rate q over the computational mesh, and the corresponding inferred convergence prefactor A. As with the 1-D Riemann problem, the prefactors are exceptionally large. Maps of the prefactor in the following figures (Figures 14a-h) show that the exceptionally high prefactors are concentrated in an area of quiescence at the top right hand corner of the computational mesh. The quiescent region contributes little to the computational error, so a more accurate measure of the mean prefactor and convergence rate would exclude the large values found in the quiescent region.

Global Convergence Results

Table 23. 2-D Riemann problem computed-estimated solution error at $t = 0.2$ s.

N_x	Δx (cm)	$\|\hat{\rho} - \rho_{\Delta x}\|_1$ (g cm^{-3})	$\|\hat{p} - p_{\Delta x}\|_1$ (dyne cm^{-2})	$\|\hat{e} - e_{\Delta x}\|_1$ (erg g^{-1})	$\|\hat{u} - u_{\Delta x}\|_1$ (cm s^{-1})
32 (64, 128)	0.03125	8.77×10^{-3}	8.791×10^{-3}	3.69×10^{-2}	2.013×10^{-2}
64 (128, 256)	0. 015625	5.703×10^{-3}	4.917×10^{-3}	2.015×10^{-2}	1.135×10^{-2}

RAGE version 2004-1126

Mean, Pointwise Convergence Results

Table 24. 2-D Riemann rarefaction problem estimated convergence rate q, $t = 0.2$ s.

Range of cells	*Density*	*Pressure*	*Energy*	*Speed*
32 (64, 128)	1.91±1.23	2.16±1.28	1.99±1.07	2.09±1.27
64 (128, 256)	2.29±1.73	2.45±1.80	2.38±1.77	2.42±1.77

RAGE version 2004-1126

Table 25. 2-D Riemann rarefaction problem estimated convergence prefactor A, t=0.2 s.

Range of cells	*Density*	*Pressure*	*Energy*	*Speed*
32 (64, 128)	$(2.33\pm65.5)\times10^{10}$	$(6.60\pm94.6)\times10^{10}$	$(2.07\pm63.8)\times10^{9}$	$(1.43\pm39.6)\times10^{9}$
64 (128, 256)	$(7.11\pm196)\times10^{20}$	$(9.95\pm274)\times10^{20}$	$(7.02\pm195)\times10^{20}$	$(2.77\pm108)\times10^{24}$

RAGE version 2004-1126

Figures 13-16 contain plots that further illuminate the results for the 2-D Riemann rarefaction problem. Figures 13a–d contain, respectively, plots of the computed solution for the density, pressure, SIE, and speed at the final time on the four computational meshes. These plots show the continuous nature of the solution, and are qualitatively reminiscent of the plots given, e.g., by Lax & Liu [Lax98] and Kamm & Rider [Kam98].[4]

Figures 14a-h each contains four plots: the estimated solution, the convergence index, the conference prefactor, and the convergence rate, all over the computational mesh for the various quantities (density, pressure, SIE, and speed) and different resolutions (32/64/128 and 64/128/256). The convergence index (upper right plot) shows graphically the convergence of points within the Newton solver. The only failure of the solver algorithm is shown by the red cells (in all figures except 14c-d) for which a zero was found in the diagonal of the upper triangular matrix. As these figure show, the Newton solver successfully converged for almost all cells where it was possible to converge. In Figures 14e-f, there are horizontal and vertical band structures in the solution; these may be due to discontinuous initial conditions. These structures can be seen to correlate to extrema in both the prefactor and convergence rate plots.

Figure 15 contains plots of the global error with the estimated solution standing in for the exact solution. Figure 16 displays the pointwise mean and standard deviation of the con-

[4] Note, however, that the solution is not smooth: at the edges of the rarefaction fan regions, the solution is continuous but not differentiable.

vergence rate and show exceptionally large uncertainty bounds, which increase with zoning refinement.

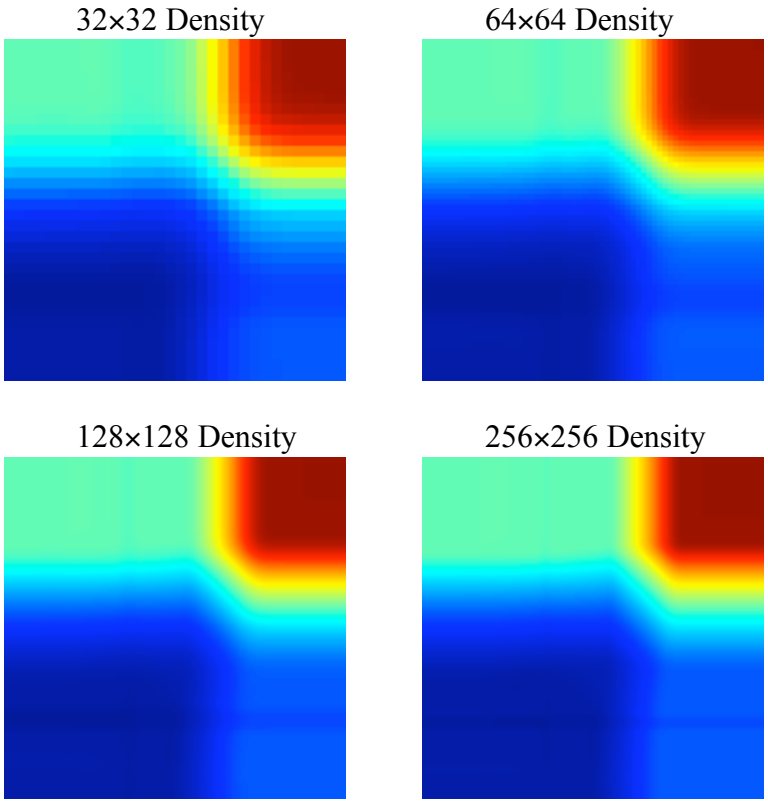

Figure 13a. Plots of the computed density for the 2-D Riemann rarefaction problem at the time $t = 0.2$ s on the four computational meshes considered. Clockwise from the upper left, the plots correspond to the 32×32, 64×64, 256×256, and 128×128 meshes on the unit square. The data range is (dark blue) $0.09 \leq \rho \leq 1.0$ (dark red). All values are in g/cm^3.

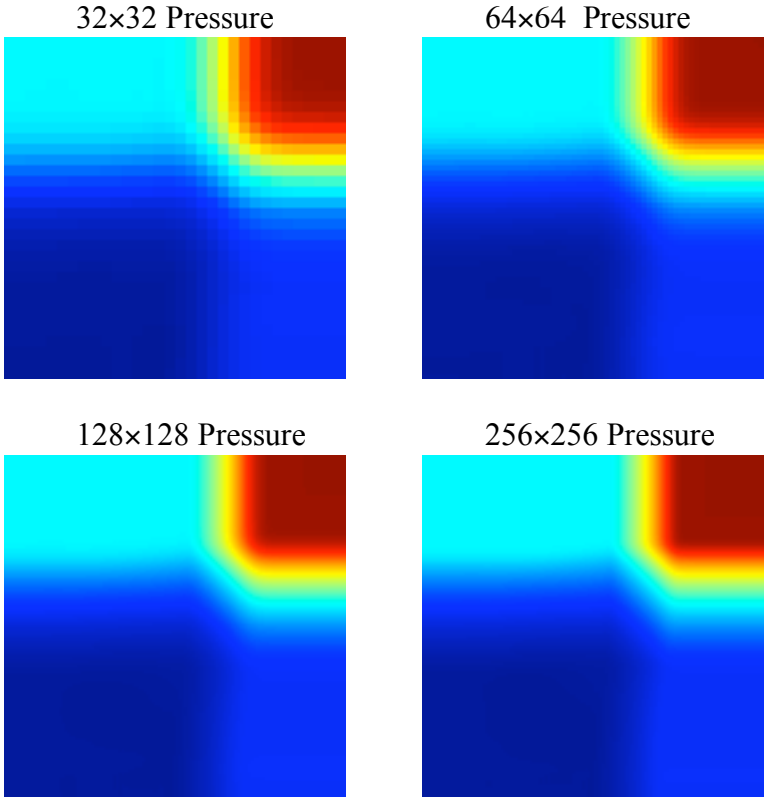

Figure 13b. Plots of the computed pressure for the 2-D Riemann rarefaction problem at the time $t = 0.2$ s on the four computational meshes considered. Clockwise from the upper left, the plots correspond to the 32×32, 64×64, 256×256, and 128×128 meshes on the unit square. The data range is (dark blue) $0.04 \leq p \leq 1.0$ (dark red). All values are in dyne/cm^2.

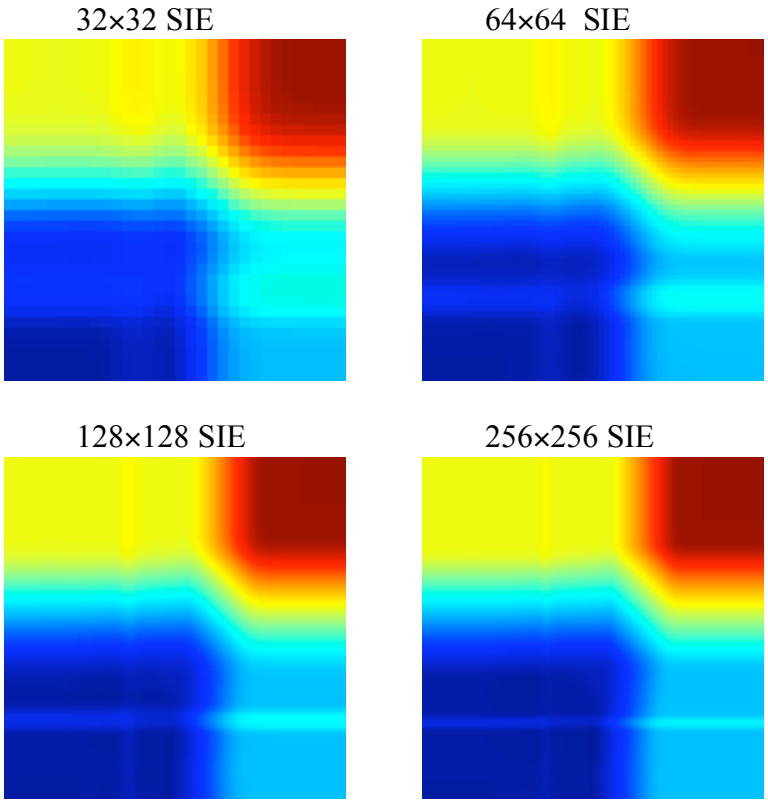

Figure 13c. Plots of the computed SIE for the 2-D Riemann rarefaction problem at the time t = 0.2 s on the four computational meshes considered. Clockwise from the upper left, the plots correspond to the 32×32, 64×64, 256×256, and 128×128 meshes on the unit square. The data range is (dark blue) $1.0 \leq e \leq 2.5$ (dark red). All values are in erg/g.

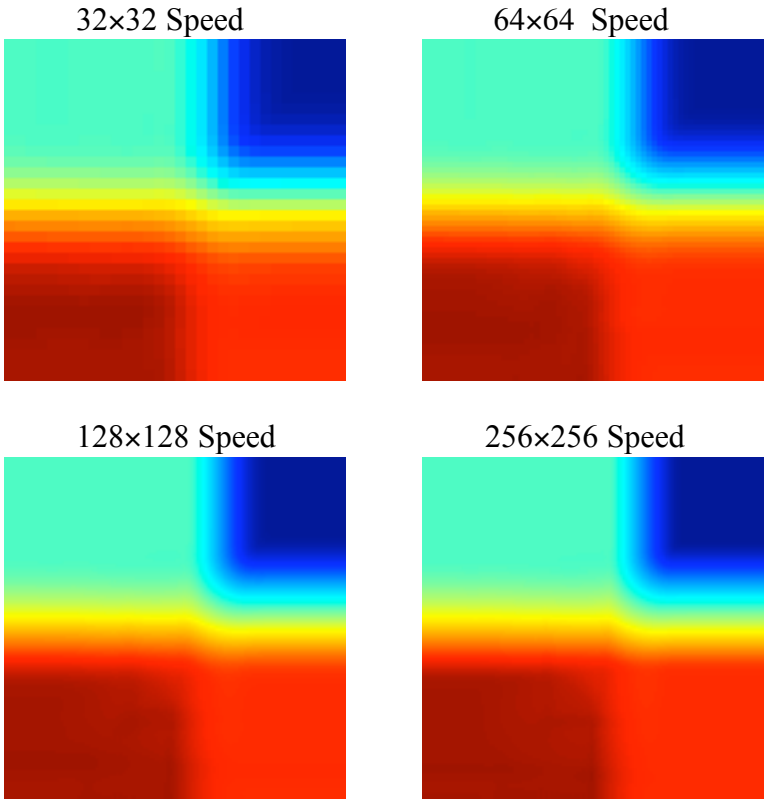

Figure 13d. Plots of the computed speed for the 2-D Riemann rarefaction problem at the time t = 0.2 s on the four computational meshes considered. Clockwise from the upper left, the plots correspond to the 32×32, 64×64, 256×256, and 128×128 meshes on the unit square. The data range is (dark blue) $0.0 \leq u \leq 1.6$ (dark red). All values are in cm/s.

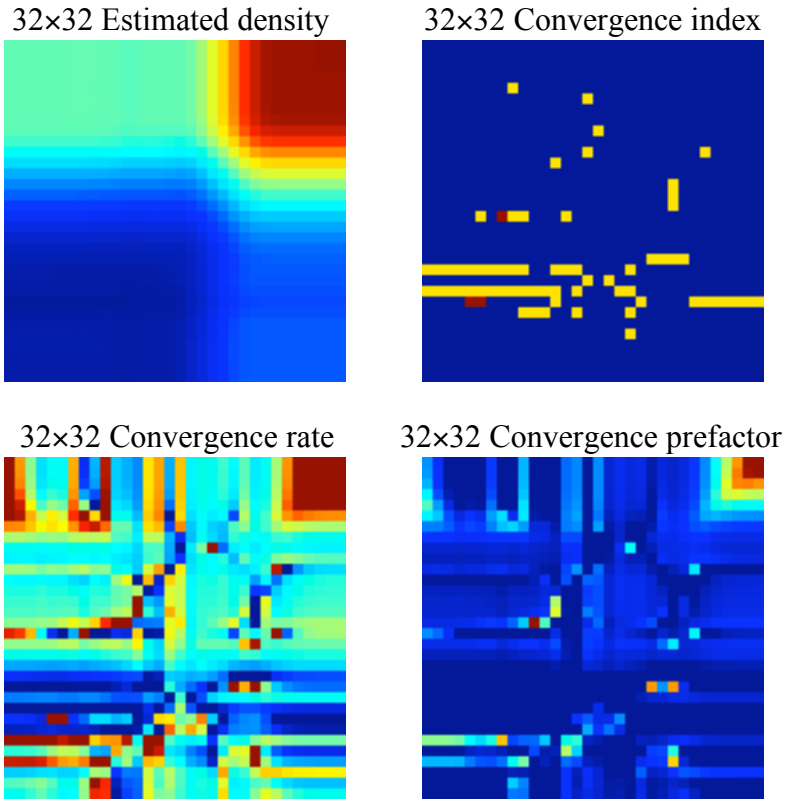

Figure 14a. Plots of the estimated quantities related to density for the 2-D Riemann rarefaction problem from the 32-, 64-, and 128-zone computational meshes at t = 0.2 s. Clockwise from the upper left, these are plots of: (i) the estimated density, on the range (dark blue) $0.09 \le \rho \le 1.0$ (dark red) in g/cm^3; (ii) Newton solver convergence index (iii) convergence prefactor A, on the logarithmic range (dark blue) $1 \le A \le 10^{10}$ (dark red); and (iv) convergence rate, on the range (dark blue) $0 \le q \le 4.0$ (dark red). The top right plot shows that the method did not converge primarily along a horizontal band approximately one-quarter up the mesh from the bottom, which we speculate corresponds to the final position of the initial discontinuity. From the plots in the bottom row, it is seen that the method converged at very high rates in the upper right corner, where essentially no evolution has taken place.

Newton solver convergence index key:
(1) Blue : Newton solver converged.
(2) Light Blue: Points with an order for which no solution exists (Eq. 2-9).
(3) Yellow: Points too close together to calculate convergence reliably.
(4) Red: A zero was in the diagonal of the U matrix and the Newton solver failed.

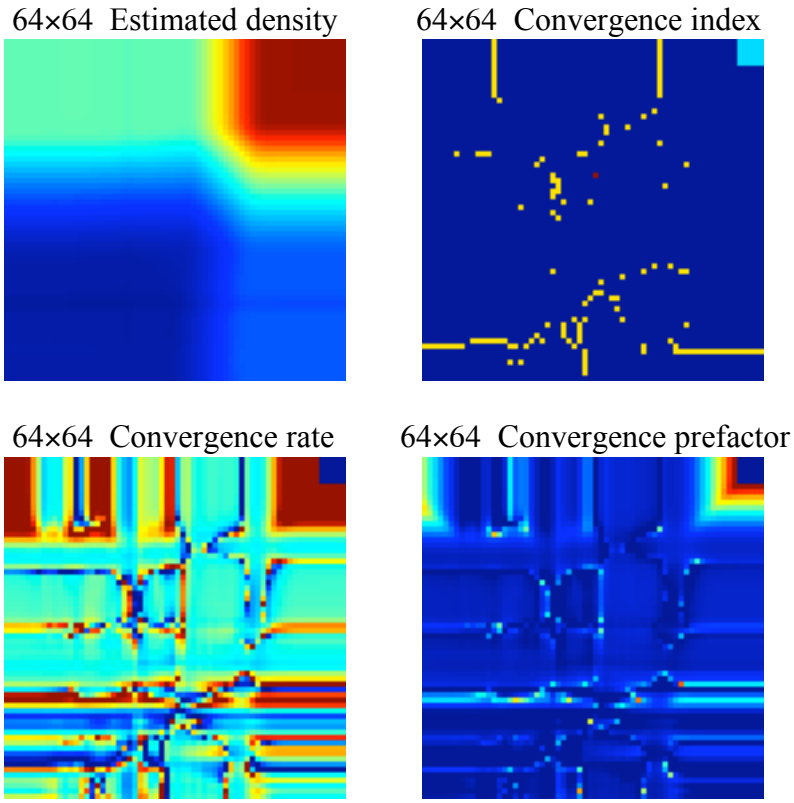

Figure 14b. Plots of the estimated quantities related to density for the 2-D Riemann rarefaction problem from the 64, 128-, and 256-zone computational meshes at t = 0.2 s. Clockwise from the upper left, these are plots of: (i) the estimated density, on the range (dark blue) $0.09 \le \rho \le 1.0$ (dark red) in g/cm^3; (ii) Newton solver convergence index (iii) convergence prefactor A, on the logarithmic range (dark blue) $1 \le A \le 10^{20}$ (dark red); and (iv) convergence rate q, on the range (dark blue) $0 \le q \le 4.0$ (dark red). The top right plot shows that the method did not converge primarily along a horizontal band near the upper boundary and along horizontal bands near the upper boundary; we speculate that these also correspond to the final position of the initial discontinuity. From the plots in the bottom row, it is seen that the method converged at very high rates in the upper right corner, the upper left corner, and along a horizontal band near $y \approx 0.25$.

Newton solver convergence index key:
(1) Blue : Newton solver converged.
(2) Light Blue: Points with an order for which no solution exists (Eq. 2-9).
(3) Yellow: Points too close together to calculate convergence reliably.
(4) Red: A zero was in the diagonal of the U matrix and the Newton solver failed.

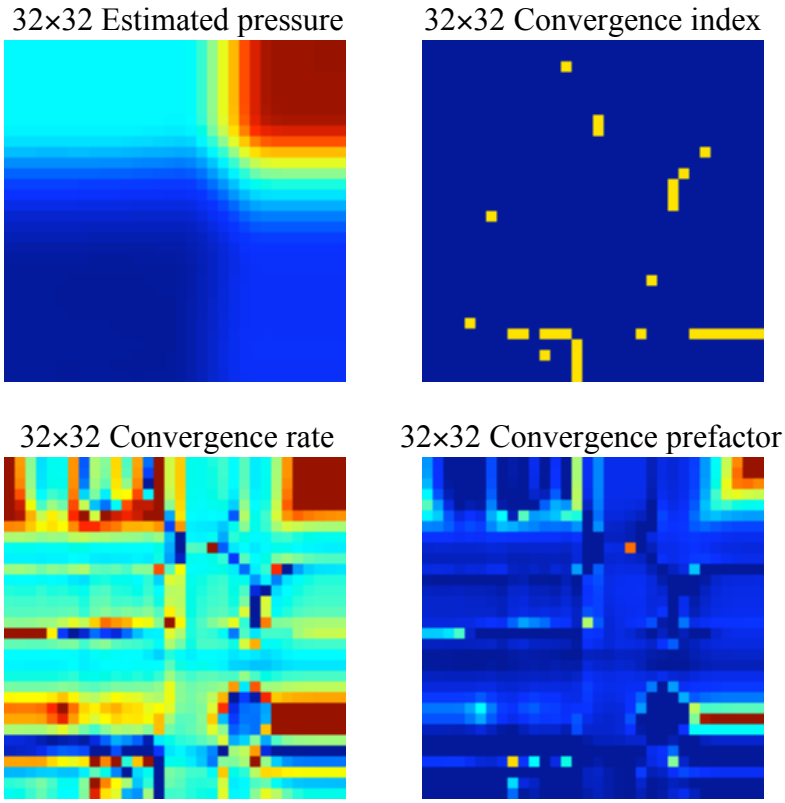

Figure 14c. Plots of the estimated quantities related to pressure for the 2-D Riemann rarefaction problem from the 32-, 64-, and 128-zone computational meshes at $t = 0.2$ s. Clockwise from the upper left, these are plots of: (i) the estimated pressure, on the range (dark blue) $0.04 \leq p \leq 1.0$ (dark red) in dyne/cm^2; (ii) Newton solver convergence index (iii) convergence prefactor A, on the logarithmic range (dark blue) $1 \leq A \leq 10^{10}$ (dark red); and (iv) convergence rate, on the range (dark blue) $0 \leq q \leq 4.0$ (dark red). The top right plot shows that the method did not converge primarily along a horizontal band approximately one-quarter up the mesh from the bottom, which we speculate corresponds to the final position of the initial discontinuity. From the plots in the bottom row, it is seen that the method converged at very high rates in the upper right corner, where essentially no evolution has taken place.

Newton solver convergence index key:
(1) Blue : Newton solver converged.
(2) Light Blue: Points with an order for which no solution exists (Eq. 2-9).
(3) Yellow: Points too close together to calculate convergence reliably.
(4) Red: A zero was in the diagonal of the U matrix and the Newton solver failed.

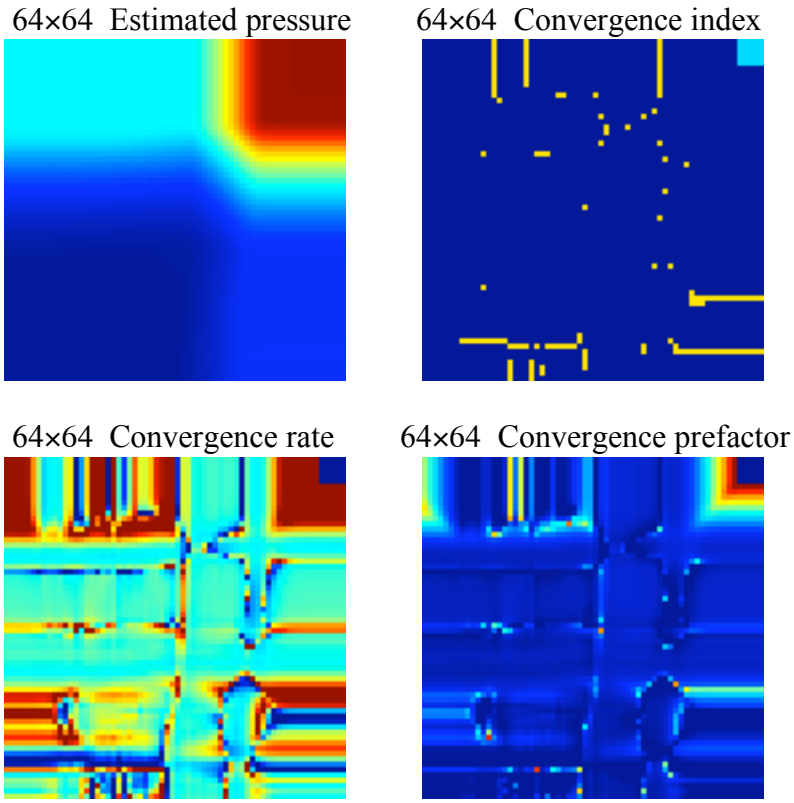

Figure 14d. Plots of the estimated quantities related to pressure for the 2-D Riemann rarefaction problem from the 64, 128-, and 256-zone computational meshes at $t = 0.2$ s. Clockwise from the upper left, these are plots of: (i) the estimated pressure, on the range (dark blue) $0.04 \le p \le 1.0$ (dark red) in dyne/cm^2; (ii) Newton solver convergence index (iii) convergence prefactor A, on the logarithmic range (dark blue) $1 \le A \le 10^{20}$ (dark red); and (iv) convergence rate q, on the range (dark blue) $0 \le q \le 4.0$ (dark red). The top right plot shows that the method did not converge primarily along a horizontal band near the upper boundary and along horizontal bands near the upper boundary; we speculate that these also correspond to the final position of the initial discontinuity. From the plots in the bottom row, it is seen that the method converged at very high rates in the upper right corner, the upper left corner, and along a horizontal band near $y \approx 0.25$.

Newton solver convergence index key:
(1) Blue : Newton solver converged.
(2) Light Blue: Points with an order for which no solution exists (Eq. 2-9).
(3) Yellow: Points too close together to calculate convergence reliably.
(4) Red: A zero was in the diagonal of the U matrix and the Newton solver failed.

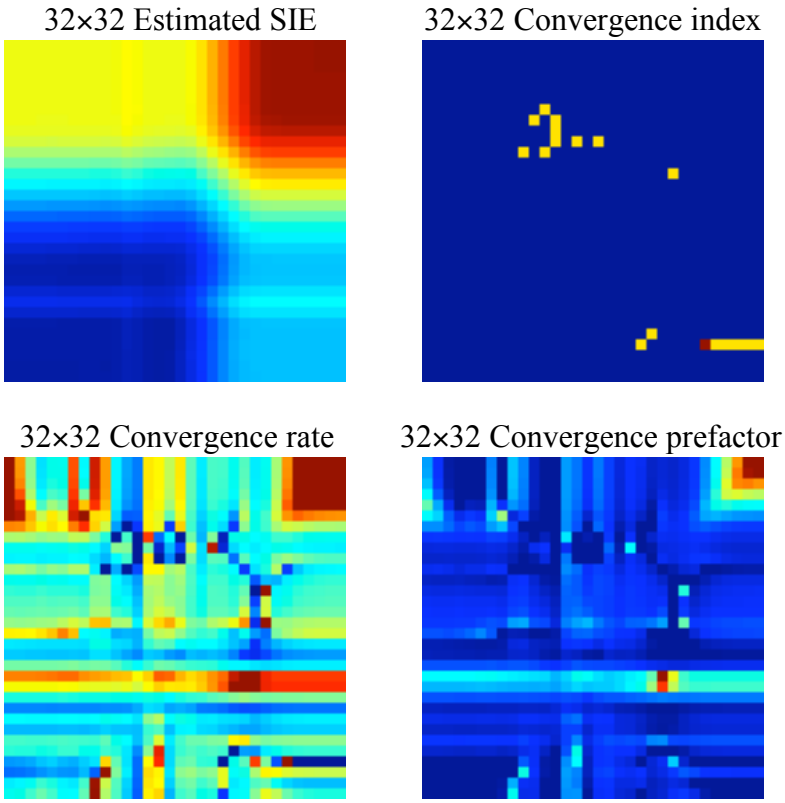

Figure 14e. Plots of the estimated quantities related to SIE for the 2-D Riemann rarefaction problem from the 32-, 64-, and 128-zone computational meshes at t = 0.2 s. Clockwise from the upper left, these are plots of: (i) the estimated SIE, on the range (dark blue) $1.0 \le e \le 2.5$ (dark red) in erg/g; (ii) Newton solver convergence index (iii) convergence prefactor A, on the logarithmic range (dark blue) $1 \le A \le 10^{10}$ (dark red); and (iv) convergence rate, on the range (dark blue) $0 \le q \le 4.0$ (dark red). The top right plot shows that the method did not converge primarily along a horizontal band approximately one-quarter up the mesh from the bottom, which we speculate corresponds to the final position of the initial discontinuity. From the plots in the bottom row, it is seen that the method converged at very high rates in the upper right corner, where essentially no evolution has taken place.

Newton solver convergence index key:
(1) Blue : Newton solver converged.
(2) Light Blue: Points with an order for which no solution exists (Eq. 2-9).
(3) Yellow: Points too close together to calculate convergence reliably.
(4) Red: A zero was in the diagonal of the U matrix and the Newton solver failed.

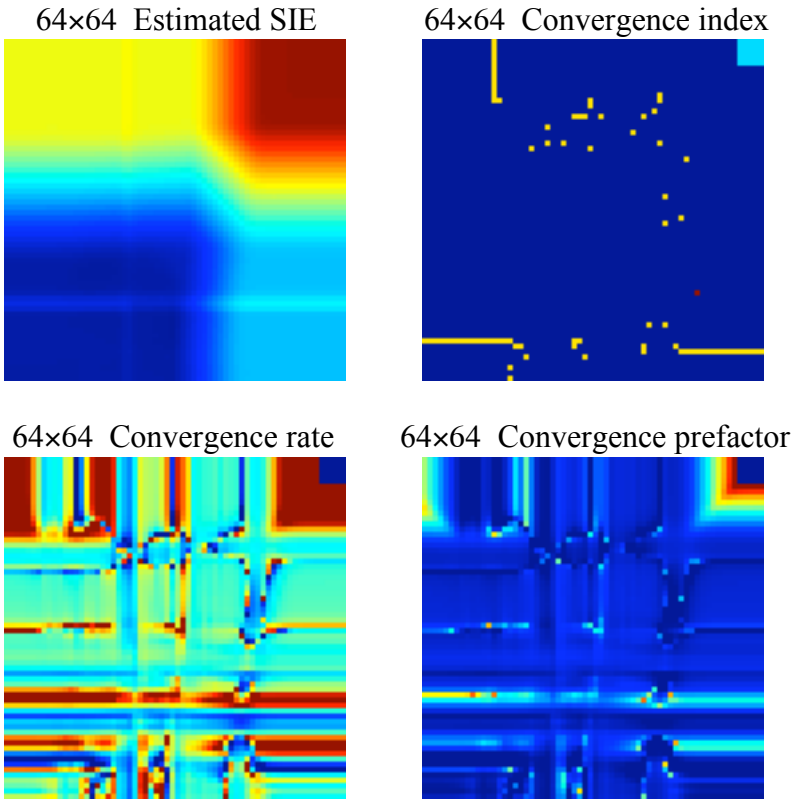

Figure 14f. Plots of the estimated quantities related to SIE for the 2-D Riemann rarefaction problem from the 64, 128-, and 256-zone computational meshes at $t = 0.2$ s. Clockwise from the upper left, these are plots of: (i) the estimated SIE, on the range (dark blue) $1.0 \le e \le 2.5$ (dark red) in erg/g; (ii) Newton solver convergence index (iii) convergence prefactor A, on the logarithmic range (dark blue) $1 \le A \le 10^{20}$ (dark red); and (iv) convergence rate q, on the range (dark blue) $0 \le q \le 4.0$ (dark red). The top right plot shows that the method did not converge primarily along a horizontal band near the upper boundary and along horizontal bands near the upper boundary; we speculate that these also correspond to the final position of the initial discontinuity. From the plots in the bottom row, it is seen that the method converged at very high rates in the upper right corner, the upper left corner, and along a horizontal band near $y \approx 0.25$.

Newton solver convergence index key:
(1) Blue : Newton solver converged.
(2) Light Blue: Points with an order for which no solution exists (Eq. 2-9).
(3) Yellow: Points too close together to calculate convergence reliably.
(4) Red: A zero was in the diagonal of the U matrix and the Newton solver failed.

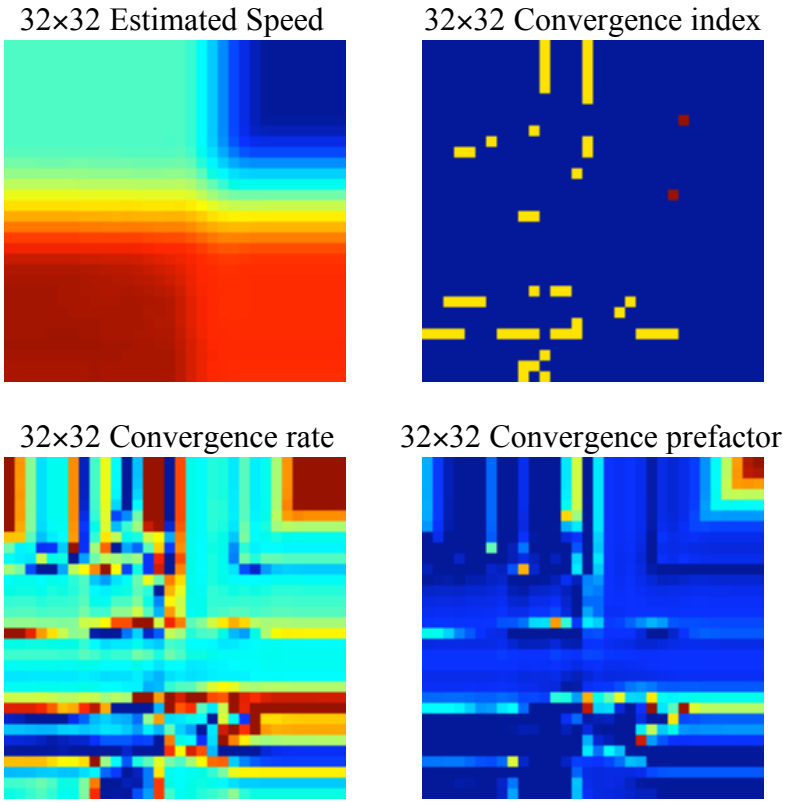

Figure 14g. Plots of the estimated quantities related to speed for the 2-D Riemann rarefaction problem from the 32-, 64-, and 128-zone computational meshes at t = 0.2 s. Clockwise from the upper left, these are plots of: (i) the estimated speed, on the range (dark blue) $0.0 \le u \le 1.6$ (dark red) in cm/s; (ii) Newton solver convergence index (iii) convergence prefactor A, on the logarithmic range (dark blue) $1 \le A \le 10^{10}$ (dark red); and (iv) convergence rate, on the range (dark blue) $0 \le q \le 4.0$ (dark red). The top right plot shows that the method did not converge primarily along a horizontal band approximately one-quarter up the mesh from the bottom, which we speculate corresponds to the final position of the initial discontinuity. From the plots in the bottom row, it is seen that the method converged at very high rates in the upper right corner, where essentially no evolution has taken place.

Newton solver convergence index key:
(1) Blue : Newton solver converged.
(2) Light Blue: Points with an order for which no solution exists (Eq. 2-9).
(3) Yellow: Points too close together to calculate convergence reliably.
(4) Red: A zero was in the diagonal of the U matrix and the Newton solver failed.

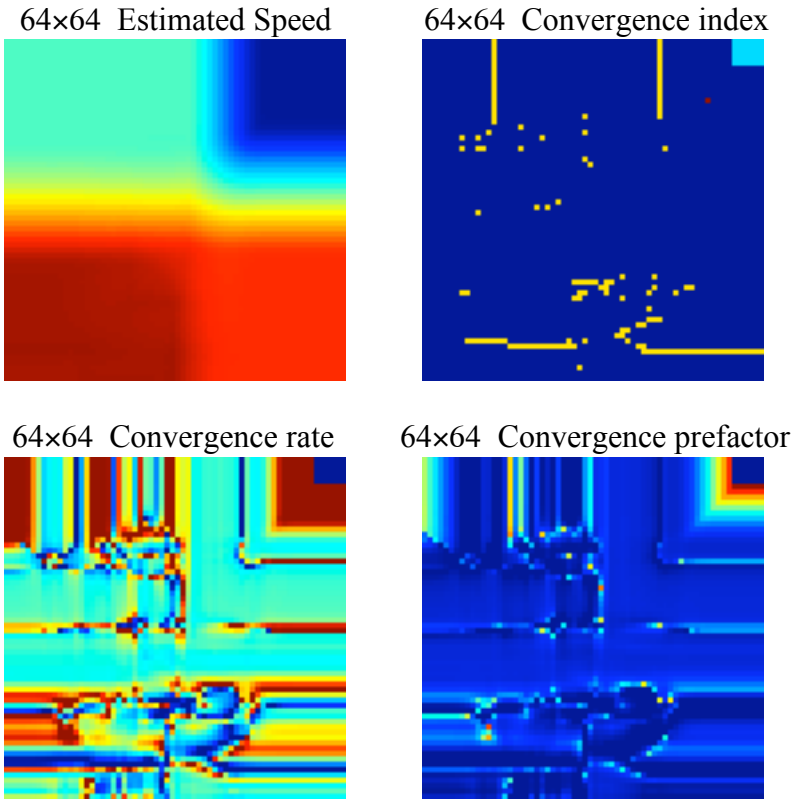

Figure 14h. Plots of the estimated quantities related to speed for the 2-D Riemann rarefaction problem from the 64, 128-, and 256-zone computational meshes at $t = 0.2$ s. Clockwise from the upper left, these are plots of: (i) the estimated speed, on the range (dark blue) $0.0 \le u \le 1.6$ (dark red) in cm/s; (ii) Newton solver convergence index (iii) convergence prefactor A, on the logarithmic range (dark blue) $1 \le A \le 10^{20}$ (dark red); and (iv) convergence rate q, on the range (dark blue) $0 \le q \le 4.0$ (dark red). The top right plot shows that the method did not converge primarily along a horizontal band near the upper boundary and along horizontal bands near the upper boundary; we speculate that these also correspond to the final position of the initial discontinuity. From the plots in the bottom row, it is seen that the method converged at very high rates in the upper right corner, the upper left corner, and along a horizontal band near $y \approx 0.25$.

Newton solver convergence index key:
(1) Blue : Newton solver converged.
(2) Light Blue: Points with an order for which no solution exists (Eq. 2-9).
(3) Yellow: Points too close together to calculate convergence reliably.
(4) Red: A zero was in the diagonal of the U matrix and the Newton solver failed.

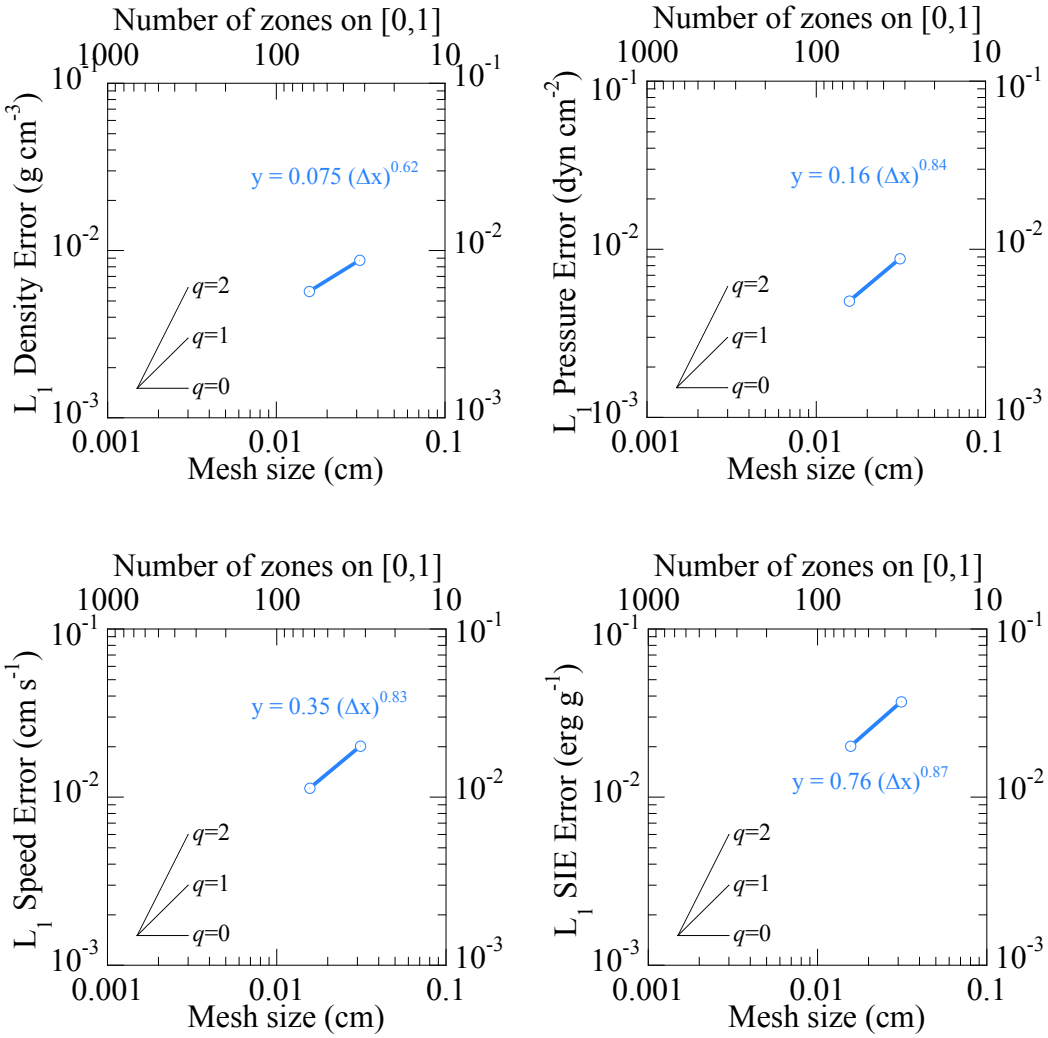

Figure 15. Plots of the effective error for the 2-D Riemann rarefaction problem at time t = 0.2 s on the two computational meshes for which the estimated solution was obtained. *Although it appears visually similar, this is a different kind of data than that shown in Figures 2 and 9.* Clockwise from the upper left, results are plotted for the density, pressure, SIE, and speed. The lines in the lower left of each plot represent convergence rates of q = 0, 1, and 2. The equation in blue gives the effective convergence relation associated with the two data points in each plot.

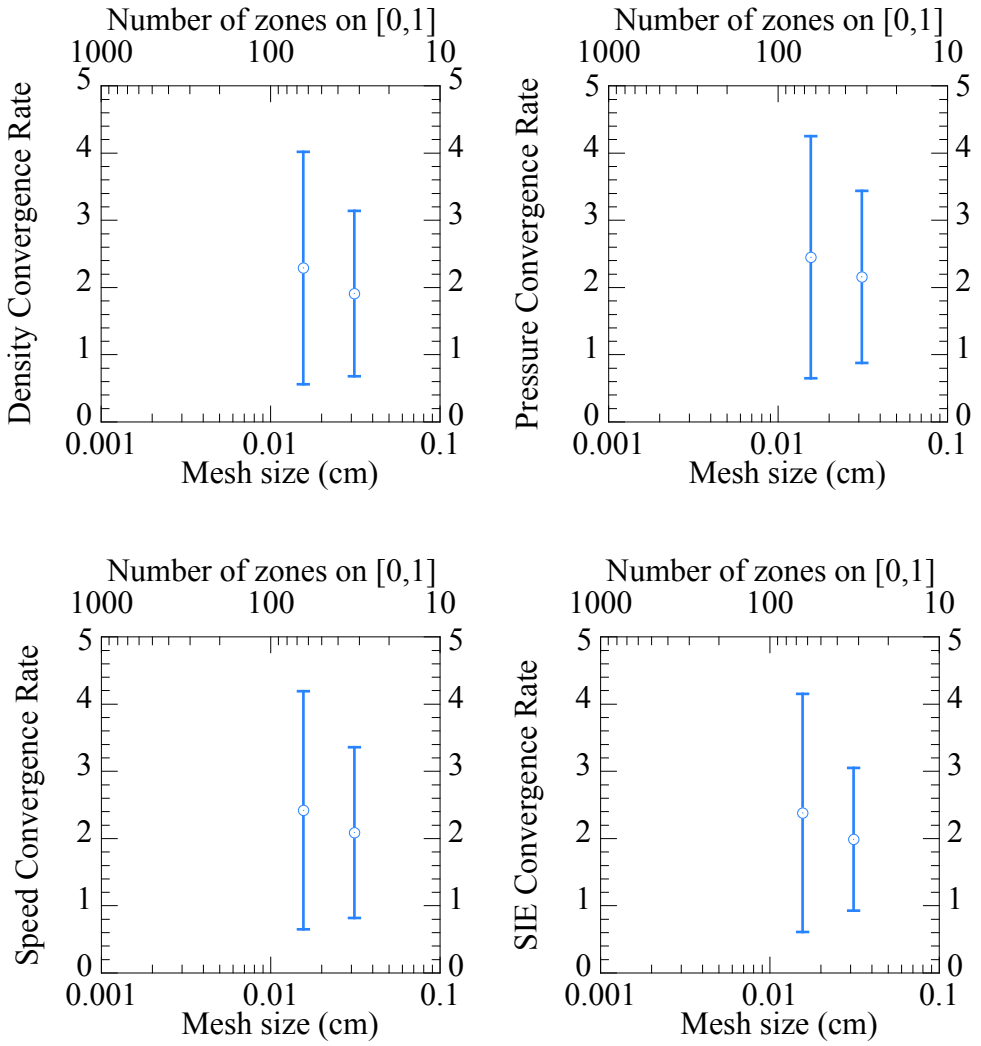

Figure 16. Plots of the mean convergence rate q for the 2-D Riemann rarefaction problem at time t = 0.2 s on the two computational meshes for which these values were obtained. Clockwise from the upper left, results are plotted for the density, pressure, SIE, and speed. The uncertainty bounds in these plots indicate ± one standard deviation in these values, which are calculated from the distribution of convergence rate values on the mesh.

5. Summary and Conclusions

We have described, implemented, and applied a method with which to gauge both an estimated solution and its asymptotic convergence properties based on a series of calculations performed on different spatial meshes. This method provides pointwise estimates of the local solution together with estimates of the uncertainty in the numerical discretization of the computed solution. This approach perforce requires several assumptions, but, as demonstrated, applies to both smooth and non-smooth solutions.

We have evaluated this process on a small set of simple 1-D and 2-D test problems, simulations for which were conducted with the RAGE code. All computational grids were uniform and a constant, forced, time step was used. Simulations without forced time step were run first, in order to determine what the size of the forced time step should be. The results attest to the efficacy of this procedure for Eulerian calculations on structured meshes. The outcome of those investigations is summarized as follows.

The 2-D linear acoustic wave problem: Global convergence was observed for this problem relative to both the exact (Table 6) and estimated (Table 9) solutions. Comparison of the exact, computed, and estimated solutions showed that the estimated solution is quite a bit better than the coarse mesh computed solution. The error between the exact and estimated solution is larger than between the exact and fine-mesh computed solution. However, we suspect that if the fine-mesh solution were averaged onto the coarse-mesh, it would have a higher error than the estimated solution. The estimated solution was found to be a function of the zoning of the three simulations used to construct it. The convergence rate and prefactor for the global, exact speed solution (Tables 6 and 7) had no discernable relationship with zone size, while the other physical quantities showed a decrease in their magnitude with zone size.

The 2-D nonlinear acoustic wave problem: This problem had no exact solution and the estimated solution replaced the exact solution for the convergence study. Error norms between the estimated and calculated solutions showed greater than second order convergence (Table 13), comparable to the linear acoustic wave problem. The global prefactor for speed for the fine calculation had an anomalously low value.

The 1-D Riemann problem: Global convergence was observed for this problem for all physical quantities, relative to both the exact (Table 17) and estimated (Table 20) solutions. The exact, global convergence rate and prefactor increased with spatial resolution for density and pressure, the opposite behavior from the 2-D linear acoustic problem. For SIE and x-velocity, there was no discernable trend, which is noteworthy. Again, the error of the estimated solution was less than the computed coarse grid solution. The graphical results of Figs. 8a and 8b demonstrate how *the estimated convergence properties can be interpreted as quantified uncertainties of the numerical discretization errors*.

The 2-D Riemann problem: Because the problem did not have an exact solution, the estimated solution was used in its place. Global error norms suggest convergence

quantified in Table 24. Importantly, the 2-D Riemann problem contained a number of points that converged in an oscillatory nature. Our method of calculating convergence *allowed oscillatory points to be included in the global convergence analysis of this problem*.

In all problems, the mean and standard deviation of the pointwise convergence rate and prefactor increased with decreasing mesh size. The behavior seemed unusual and may be the result of a few outlying points that skewed the averages.

The results on this study demonstrate the capacity of our method to obtain solutions that more faithfully resolve solution discontinuities. Overall, the procedure we propose appears to operate robustly on 1- and 2-D smooth and discontinuous problems. We draw this conclusion based on the results discussed in this section, namely, that (i) the procedure converges on a large fraction of the mesh points, (ii) the estimated solution provides an estimate of the exact solution that is quantitatively superior to the computed solution on the same mesh, and (iii) the computed convergence characteristics (rate and prefactor) provide reasonable bounds for the numerical discretization properties of the calculated solution.

As a result of this study, we suggest that the following actions be considered.

• Investigate the non-uniqueness of the computed solution. This approach depends on the solution to a set of nonlinear equations (Eq. 2-4), which may possess several solutions. It would be of interest to apply more sophisticated numerical techniques in an effort to obtain *all* solutions of these equations, to develop some confidence that the inferred solutions are indeed appropriate.

• Exercise this approach on coupled mutiphysics problems. An important outcome of this approach is to provide estimates of the solution (and consistent discretization error measures) irrespective of the underlying equations. Coupled multiphysics problems—for which few exact solutions exist—provide cases that are ideally situated to benefit from this technique.

• Enhance the error ansatz. This could be undertaken by replacing the error relation we have assumed (e.g., Eq. (3-1)) with a more advanced error model, e.g., including temporal discretization error [Kam02] or a more sophisticated ansatz [Hem05]. Such extensions would require modification of the solution technique (i.e., the Newton's method used in this study), but are otherwise straightforward.

• Extend this approach to non-uniform meshes. This nontrivial extension would require both careful interpolation (i.e., conservative remap) procedures and characterization of appropriate length scales (represented as Δx in the error ansatz). Whereas the necessary remapping techniques may be at hand, the thorny issue of proper length scale characterization remains, to the authors' knowledge, unresolved (perhaps it could be circumvented by modifying the error ansatz to be independent of the length scale).

• Incorporate this method into an automated analysis toolbox. The analysis we have presented could be incorporated into the analysis frameworks presently being developed, e.g., the Pinocchio project [Hrb05] or AMHC_Tools [Gro05]. The inclusion of this method into such a toolbox would allow convenient application of this approach to a spectrum of problems by a larger set of users and analysts.

Acknowledgements This work was performed by Los Alamos National Laboratory, which is operated by the University of California for the National Nuclear Security Administration of the U.S. Department of Energy under contract W-7405-ENG-36. The authors acknowledge the kind support of the LANL ASC V&V Program and its manager, Scott Doebling. We appreciate the ongoing and stimulating technical interactions on verification-related issues with our Verification Project team members, in particular, François Hemez and Bill Rider. The constructive and insightful feedback of these colleagues on early drafts of this report is gratefully acknowledged.

Appendix A. Evaluation of Solution Norms

This appendix contains a very brief discussion of the implementation of the error norms in these expressions. The definition of the L_p norm of the function f defined on the set Ω contained in the space of n-tuples of real numbers is

$$\|f\|_p = \left[\frac{1}{\mu(\Omega)} \int_\Omega d^n\boldsymbol{x} \; |f(\boldsymbol{x})|^p \right]^{1/p}, \tag{A-1}$$

where $\mu(\Omega)$ is the measure of the set Ω (e.g., the length $\mathcal{L}$ in 1-D, the area $\mathcal{A}$ in 2-D or the volume $\mathcal{V}$ in 3-D). The expression of the element $d^n\boldsymbol{x}$ depends the coordinates chosen, which is simplified in this study, as we consider only Cartesian geometry. Based on these definitions, the L_1 and L_2 norms are defined as

$$\|f\|_1 = \left[\frac{1}{\mu(\Omega)} \int_\Omega d^n\boldsymbol{x} \; |f(\boldsymbol{x})| \right] \quad \text{and} \tag{A-2}$$

$$\|f\|_2 = \left[\frac{1}{\mu(\Omega)} \int_\Omega d^n\boldsymbol{x} \; |f(\boldsymbol{x})|^2 \right]^{1/2}. \tag{A-3}$$

The specific coordinate systems we consider in this report include 1-D and 2-D Cartesian coordinates, so the definitions of the spatial elements ($d^n\boldsymbol{x}$) and integration domains are straightforward.

The expressions in Eqs. (A-2) and (A-3) are evaluated using approximations based on the corresponding discretized values on the computational mesh. The following simple quadrature rule is used in these evaluations:

$$\int_\Omega d^n\boldsymbol{x} \; f(\boldsymbol{x}) \approx \sum_i f(\boldsymbol{x}_i) \; \Delta^n\boldsymbol{x}_i \quad \text{and} \quad \mu(\Omega) \approx \sum_i \Delta^n\boldsymbol{x}_i \; . \tag{A-4}$$

References

AIAA98, *Guide for the Verification and Validation of Computational Fluid Dynamics Simulations*, AIAA Guide G-077-1998, 1998.

ASME04, ASME PTC60 Committee on Verification and Validation in Computational Solid Mechanics, *Guide for the Verification and Validation in Computational Solid Mechanics (Draft),* 22 March 2004 (unpublished).

Cad02, Cadafalch, J., Pérez-Segarra, C.C., Cònsul, R., Oliva, A., Verification of Finite Volume Computations on Steady-State Fluid Flow and Heat Transfer, *J. Fluids Eng*., **24**, pp. 11–21, 2002.

Col97, Coleman, H.G., Stern, F., Uncertainties in CFD Code Validation, *ASME J. Fluids Eng.*, **119**, pp. 795–803, 1997.

Col98, Coleman, H.G., Stern, F., Authors' Closure, *ASME J. Fluids Eng.*, **120**, pp. 935–636, 1998.

Eng98, Engquist, B., Sjögreen, B., The convergence rate of finite difference schemes in the presence of shocks, *SIAM J. Num. Anal*., **35**, pp. 3464–2485, 1998.

Got88, Gottlieb, J.J., Groth, C.P.T., Assessment of Riemann solvers for unsteady one-dimensional inviscid flows of perfect gases, *J. Comp. Phys*., **78**(2), pp. 437–458, 1988.

Gro05, Grove, J., Personal communication.

Hag88, Hager, W.W., *Applied Numerical Linear Algebra*, Prentice Hall, p.131, 1988.

Hem05, Hemez, F. M., *Nonlinear Error Ansatz Models for Solution Verification in Computational Physics*, Los Alamos National Laboratory Report LA-UR-?, 2005, to be published.

Hrb05, Hrbek, G. Personal communication.

IEEE98, *IEEE Standard for Software Verification and Validation*, IEEE Std 1012-1998 (1998).

Kam98, Kamm, J.R., Rider, W.J., *2-D Convergence Analysis of the RAGE Hydrocode*, Los Alamos National Laboratory Report LA-UR-98-3872, 1998.

Kam02, Kamm, J.R., Rider, W.J., Brock, J.S., *Consistent Metrics for Code Verification*, Los Alamos National Laboratory Report LA-UR-02-3794, 2002.

Kam03, Kamm, J.R., Brock, J.S., Rousculp, C.L., Rider, W.J., *Verification of an ASCI Shavano Project Hydrodynamics Algorithm*, Los Alamos National Laboratory Report LA-UR-03-6999, 2003.

Kim95, Kimoto, P.A., Cherno, D.F., Convergence properties of finite-difference hydrodynamics schemes in the presence of shocks, *Ap. J. Supp. Ser*., **96**, pp. 627–641, 1995.

Knu03, Knupp, P., Salari, K., *Verification of Computer Codes in Computational Science and Engineering*, Chapmann & Hall/CRC Press, Boca Raton, FL, 2003.

Lan87, Landau, L.D., Lifschitz, E.M., *Fluid Mechanics*, Butterworth-Heinemann, Oxford and Boston, (1987).

Lax98, Lax, P.D., Liu, X.-D., Solution of Two-Dimensional Riemann Problems of Gas Dynamics by Positive Schemes, *SIAM J. Sci. Comput.* **19**(2), pp. 319–340 (1998).

NCSa, *HDF 4.1r3 Reference Manual*, National Center for Supercomputing Applications, University of Illinois at Urbana-Champaign, **http://hdf.ncsa.uiuc.edu//doc.html.**

NCSb, *HDF 4.1r3 User's Guide*, National Center for Supercomputing Applications, University of Illinois at Urbana-Champaign, **http://hdf.ncsa.uiuc.edu//doc.html.**

Obe03, Oberkampf, W.L., Trucano, T.G., Hirsch, C., *Verification, Validation, and Predictive Capability in Computational Engineering and Physics*, Sandia National Laboratories Report SAND2003-3769, 2003.

Pre92a, Press, W.H., Teukolsky, S.A., Vetterling, W.T., Flannery, B.P., *Numerical Recipes in FORTRAN: The Art of Scientific Computing*, Second Edition, Cambridge University Press, New York, NY, p. 372, 1992.

Pre92b, Press, W.H., Teukolsky, S.A., Vetterling, W.T., Flannery, B.P., *Numerical Recipes in FORTRAN: The Art of Scientific Computing*, Second Edition, Cambridge University Press, New York, NY, p. 376, 1992.

Qua03, Quartapelle, L., Castelletti, L., Guardone, A., Quaranta, G., Solution of the Riemann problem of classical gasdynamics, *J. Comp. Phys.* **190**, pp. 118–140 (2003).

Roa98a, Roache, P., Verification of Codes and Calculations, *AIAA Journal*, **36**(5), pp. 696–702, 1998.

Roa98b, Roache, P., Quantification of Uncertainty in Computational Fluid Dynamics, *Annu. Rev. Fluid Mech.*, **29**, pp. 123–160, 1998.

Roa98c, Roache, P., *Verification and Validation in Computational Science and Engineering*, Hermosa Publishers, Albuquerque, NM, 1998.

Roa02, Roache, P., Code Verification by the Method of Manufactured Solutions, *Transactions of the ASME*, **124**, pp. 4–10, 2002.

Roy05, Roy, C.J., Review of code and solution verification procedures for computational simulation, *J. Comp. Phys.*, **205**, pp. 131–156, 2005.

Sal00, Salari, K., Knupp, P., *Code Verification by the Method of Manufactured Solutions*, Sandia National Laboratories Report SAND2000-1444, 2000.

Sch93a, Schulz-Rinne, C.W., Classification of the Riemann Problem for Two-dimensional Gas Dynamics, *SIAM J. Math. Anal.*, **24**, pp. 76–88 (1993).

Sch93b, Schulz-Rinne, C.W., Collins, J.P., Glaz, H.M., Numerical solution of the Riemann Problem for Two-dimensional Gas Dynamics, *SIAM J. Sci. Comput.*, **14**, pp. 1394–1414 (1993).

Tru03, Trucano, T.G., Pilch, M., Oberkampf, W.L., *On the Role of Code Comparisons in Verification and Validation*, Sandia National Laboratories Report SAND2003-2752, 2003.

Whi74, Whitham, G.B., *Linear and Nonlinear Waves*, John Wiley & Sons, New York, NY, 1974.